



Petrology, geochemistry, and correlation of tephra deposits from a large early-Holocene eruption of Mentolat volcano, southern Chile



D.J. Weller^{a,*}, M.E. de Porras^b, A. Maldonado^{c,d}, C. Méndez^e, C.R. Stern^a

^a Department of Geological Sciences, University of Colorado, Boulder, CO, 80309-0399, USA

^b Instituto Argentino de Nivología, Glaciología y Ciencias Ambientales (IANIGLA), CONICET, CCT Mendoza, Av. Ruiz Leal s/n, Mendoza, Argentina

^c Centro de Estudios Avanzados en Zonas Áridas (CEAZA), Instituto de Investigación Multidisciplinario en Ciencia y Tecnología, Universidad de La Serena, Avda. Raúl Bitrán, 1305, La Serena, Chile

^d Departamento de Biología Marina, Universidad Católica del Norte, Larrondo, 1281, Coquimbo, Chile

^e Centro de Investigación en Ecosistemas de la Patagonia (CIEP), Moraleda 16, Coyhaique, Chile

ARTICLE INFO

Keywords:

Andean volcanism
Tephra
Tephrochronology
Mentolat volcano
Chile
Patagonia

ABSTRACT

Two correlated tephra deposits, each 13 cm thick in the Aisén region of southern Chile, one in a lacustrine sediment core from the Mallín el Toqui (MET) peat bog and another from a subaerial soil exposure ~10 km to the west in the Río Maniguales (RM) valley, preserve evidence for a large explosive eruption of Mentolat volcano, one of the five stratovolcanoes of the southernmost portion of the Andean Southern Volcanic Zone (SVZ). This eruption is constrained in age to $\geq 11,728$ cal years BP by radiocarbon dating of organic matter from the MET sediment core and is termed the ~11.7 ka MEN event. The two tephra deposits are identical and based on their petrology, bulk tephra, glass, and amphibole geochemical characteristics, are attributed to an eruption of Mentolat volcano. Both contain pumice lapilli with glass compositions that ranges from 59 to 76 wt. % SiO₂, with medium to low-K₂O calc-alkaline composition and trace element abundances similar to both lavas and other tephra derived from Mentolat. They have abundant amphibole, plagioclase, orthopyroxene, and clinopyroxene phenocrysts, with a smaller proportion of olivine and Fe-Ti oxides, and a minor amount of distinctive crustal xenoliths with both unfoliated and foliated textures. Amphiboles have low K₂O (0.20–0.37 wt. %) and TiO₂ (1.5–3.8 wt. %) and are similar geochemically to amphiboles from other Mentolat-derived tephra (K₂O = 0.14–0.43 wt. % and TiO₂ = 1.9–2.4 wt. %), but distinct from amphiboles in lavas and tephra derived from other volcanoes in the southernmost SSVZ including Cay (K₂O = 0.47–0.55 wt. % and TiO₂ = 2.4–3.1 wt. %) and Melimoyu (K₂O = 0.39–0.52 wt. % and TiO₂ = 2.8–4.5 wt. %). Amphiboles from the ~11.7 ka MEN tephra formed over a broad range of pressures (154–406 MPa), temperatures (834–969 °C), and magma water contents (4.9–7.0 wt. %), which overlap with the physical-chemical conditions for the formation of amphiboles from other Mentolat-derived tephra. The two correlated tephra deposits, which are located ~95 km southeast of Mentolat, are correlative with tephra of similar age identified in 12 other lacustrine sediment cores from the region, for which, based on their petrology and the geochemistry of their tephra glass and amphiboles, Mentolat is also the likely source volcano. This eruption produced approximately 1.8 km³ of bulk material with an estimated magnitude of 5.2. Mentolat has produced numerous (> 18) explosive eruptions since glacial retreat from the region and future explosive eruptions from this center could potentially impact local population centers and the agricultural industry in southern Chile and Argentina.

1. Introduction

Explosive volcanic eruptions can disperse tephra over large areas nearly instantaneously. Once the tephra glass and mineral chemistry are characterized, and an age of the eruptive event is constrained, correlative tephra deposits can be used as an isochron (surface of equal age; Lowe, 2011) and their age transferred to other locations and

depositional environments where the tephra has been newly identified (Fontijn et al., 2014; Lowe, 2011). Explosive eruptions of the volcanoes in the Andean Southern Volcanic Zone (SVZ; Fig. 1) have produced a rich, but incompletely studied, tephra record. Tephra deposits produced by explosive eruptions of the volcanoes in the southern Andes have been used to constrain the timing of regionally significant events identified from studies of paleoclimate (e.g. Bendle et al., 2017; Elbert

* Corresponding author.

E-mail address: derek.weller@colorado.edu (D.J. Weller).

<https://doi.org/10.1016/j.jsames.2018.12.020>

Received 2 July 2018; Received in revised form 12 December 2018; Accepted 20 December 2018

Available online 24 December 2018

0895-9811/ © 2018 Elsevier Ltd. All rights reserved.

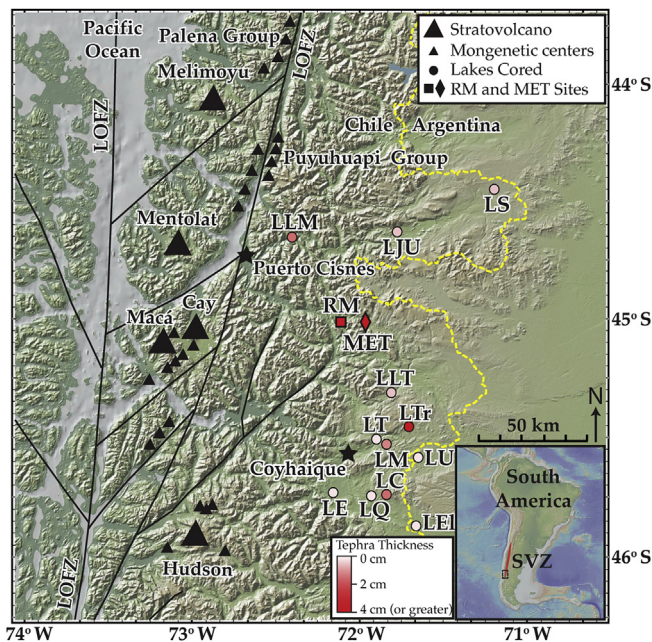


Fig. 1. A. Map showing the location of Mallín el Toqui (MET; diamond) from which the tephra bearing core was obtained and the tephra outcrop located in the Río Maniguales (RM) valley (square). Also shown are the locations of the major volcanic centers of the southern part of the Andean Southern Volcanic Zone (SSVZ) and minor eruptive centers (MEC) located along the Lliquiñe-Ofqui fault zone (LOFZ) and surrounding Hudson (Gutiérrez et al., 2005; Vargas et al., 2013), Macá, and Cay (D’Orazio et al., 2003; López-Escobar et al., 1995a), and of other tephra-bearing lake cores further to the south near Coyhaique (LLT: Laguna La Trapananda; LTr: Lake Tranquilo; LM: Lake Las Mellizas; LT: Lake Toro; LU: Lake Unco; LC: Lake Churrasco; LQ: Lake Quijada; LE: Lake Espejo; LEL: Lake Élida; Weller et al., 2018, 2015) and north in the Río Cisnes valley (LLM: Laguna Las Mellizas; LJU: Laguna Junco; LS: Lake Shaman; de Porras et al., 2012; Stern et al., 2015; Weller et al., 2017). The approximate thicknesses in these other cores of the tephra produced by the $\geq 11,728$ cal years BP early Holocene Mentolat eruption (tephra Q1 in the nine cores from near Coyhaique, tephra Q in the two cores from the lower Río Cisnes valley, and tephra M from the core in the upper Río Cisnes valley) is indicated by the degree of shading for weak (thin; < 2 cm) to strong (thicker; > 4 cm). Map was constructed using GeoMapApp (<http://www.geomapp.org>).

et al., 2013; Van Daele et al., 2016), paleoecology (e.g. de Porras et al., 2014, 2012), and archeology (e.g. Martin et al., 2015; Prieto et al., 2013). The identification and characterization of tephra layers preserved in outcrops and lacustrine sediment cores also provide constraints on volcanic risks and hazards in the region (Alloway et al., 2017; Naranjo et al., 2017; Naranjo and Stern, 2004; Rawson et al., 2015; Watt et al., 2011b), where recent volcanic eruptions have disrupted airline traffic and negatively impacted local population centers and the agricultural industry (Wilson et al., 2012, 2011).

Small internally drained lacustrine environments located downwind of the SVZ volcanoes have been shown to be ideal environments for the preservation of both small and large volcanic air fall deposits due to the nearly continuous record of sedimentation since glacial retreat of the region initiating at $\sim 18,000$ cal year BP (Bendle et al., 2017). This paper presents the age, petrology, and geochemistry of two geochemically identical ~ 13 cm thick tephra deposits, one observed in a sediment core (Fig. 2) from the Mallín el Toqui (MET) peat bog and the other in a road cut outcrop (Fig. 3) ~ 10 km to the west in the Río Maniguales (RM) valley (Fig. 1). Based on the location of these deposits, lithostratigraphic information (tephra grain size and thickness), glass major and trace element characteristics, and amphibole thermobarometry and geochemistry, we suggest that they were likely derived from a large explosive eruption of Mentolat volcano, located ~ 95 km to the northwest. They are correlative with other Mentolat-derived

Mallín El Toqui (MET) 0115A

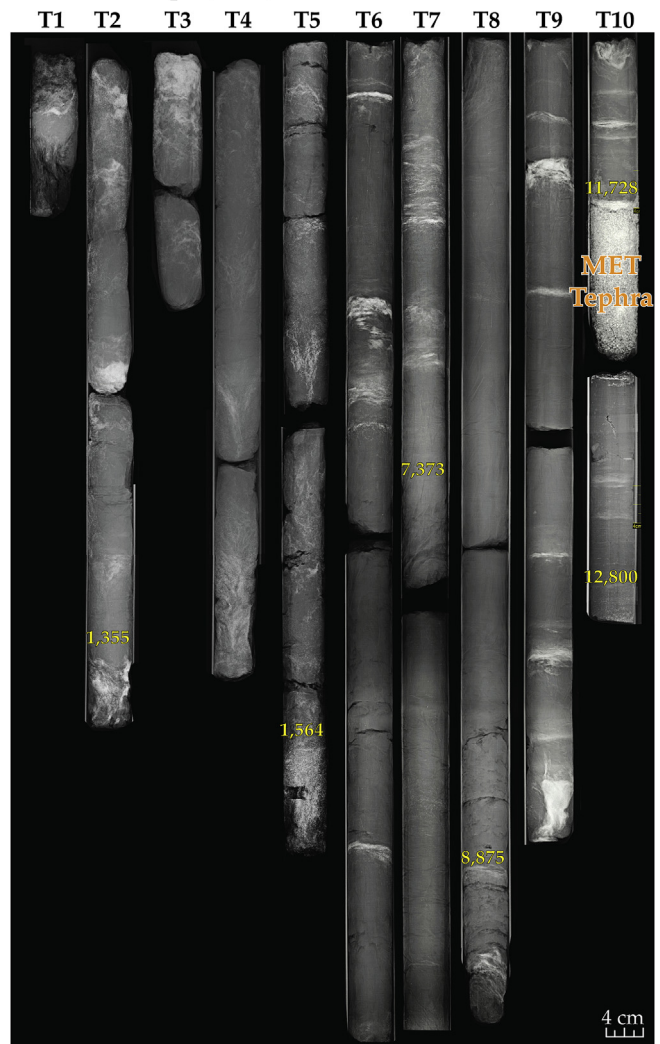


Fig. 2. Transmitted X-ray image of the 6.5-m-long core from Mallín el Toqui (MET). The dark material is the predominately organic matter rich lacustrine sediments and the white layers, or denser lithologies, are tephra layers. Except for the ~ 13 cm thick tephra layer near the middle of core section T10, the other tephra layers in the core are either too thin to be sampled or are mixed in with organic matter. Location in the core of radiocarbon age dates (in cal years BP; Table 8) are also shown.

tephras of similar age previously reported from the region (Table 1; Stern et al., 2015; Weller et al., 2017, 2015). Because they were derived from a relatively large eruption and have a wide regional depositional area, these deposits have the potential to be a significant chronological marker deposit for future paleoclimate, paleoecologic and archaeological studies in the region. They also provide information on the chemical variability of the eruptive products from Mentolat, indicating that magmas formed beneath this volcano may have followed distinct diversification pathways leading to greater chemical diversity in the evolved eruptive material than has been previously reported.

1.1. Geologic background

The Andean Southern Volcanic Zone (SVZ; inset in Fig. 1) is a 1400-km-long volcanic chain located along the western margin of the South American Plate. It consists of greater than 60 Quaternary composite volcanoes, at least 3 large caldera complexes and numerous monogenetic eruptive centers (MEC; Stern, 2004). Andean SVZ volcanoes, which occur in both Chile and Argentina, result from the subduction of

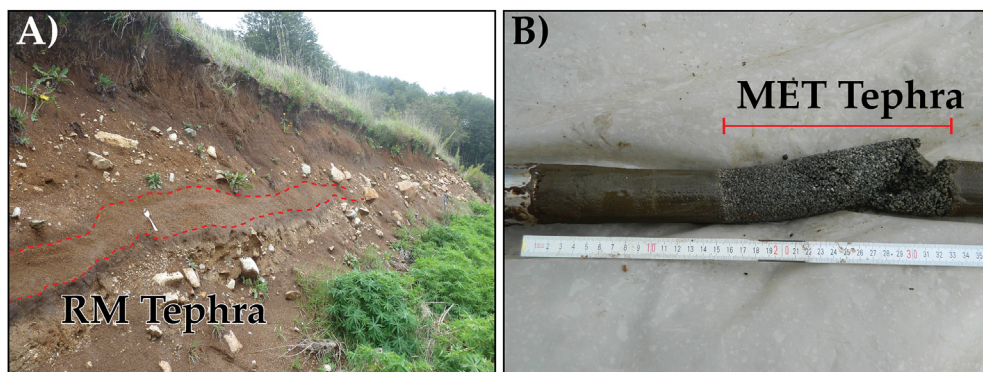


Fig. 3. Photograph of the ~13 cm thick tephra in the outcrop located in the Río Maniguales (RM) valley (A; note the spoon for scale), and (B) from the MET lake sediment core. White pumice lapilli in the lake sediment core are primarily located near the base of the deposit, indicating this was an early component of the eruptive event. They clearly fine upwards in the MET core deposit, and less obviously so in the RM outcrop, but are randomly mixed with other tephra components throughout both deposits.

Table 1

Summary of the features of the MET core and RM outcrop tephtras and features of correlated tephtras from other lacustrine sediment cores.

Location	Region	Other names	Thickness (cm)	max grain size (mm)	Age (cal yrs BP)	1 σ	Reference
Mallín el Toqui (MET)	Mallín el Toqui	–	13	7.1	> 11, 728	–	This study
Río Maniguales (RM)	Río Maniguales valley	–	13	13.0	–	–	This Study
Laguna La Trapananda (LLT)	Coyhaique	Q1	1.5	–	11,142	778	Weller et al. (2018)
Lake Tranquilo (LTr)	Coyhaique	Q1	9	2.5	–	–	Weller et al. (2015)
Lake Las Mellizas (LM)	Coyhaique	Q1	1	0.6	–	–	Weller et al. (2015)
Lake Churrasco (LC)	Coyhaique	Q1	2	0.4	–	–	Weller et al. (2015)
Lake Unco (LU)	Coyhaique	Q1	< 1	–	–	–	Weller et al. (2015)
Lake Espejo (LE)	Coyhaique	Q1	< 1	–	–	–	Weller et al. (2015)
Lake El Toro (LT)	Coyhaique	Q1	< 1	–	–	–	Weller et al. (2015)
Lake Quijada (LQ)	Coyhaique	Q1	< 1	–	–	–	Weller et al. (2015)
Lake Éliida (LEI)	Coyhaique	Q1	< 1	–	–	–	Weller et al. (2015)
Laguna Las Mellizas (LLM)	Río Cisnes valley	Q	2	4.3	–	–	Weller et al. (2017)
Laguna Junco (LJ)	Río Cisnes valley	Q	1	–	–	–	Weller et al. (2017)
Lake Shaman (LS)	Río Cisnes valley	M	1	0.9	11,140	–	Stern et al. (2015)

the Nazca Plate beneath South America at a relative convergence rate of ~7 cm/yr (DeMets et al., 2010). The southern boundary of the SVZ is at 46°S where the Chile Rise, an active spreading center separating the Nazca and Antarctic plates, enters the trench creating the Chile Rise Triple Junction. Due to the slight oblique subduction of the Nazca Plate and the nearly orthogonal subduction of the Antarctic Plate, the Chile Rise Triple Junction, that collided with the southern point of South America in the Miocene, has migrated north along the continental margin over the last 15–20 Ma (Cande et al., 1987; Cande and Leslie, 1986). South of the Chile Rise Triple Junction is a 350 km gap in the active volcanism between the SVZ and the Austral Volcanic Zone (AVZ; Stern, 2004).

The SVZ has been subdivided into four segments based on the geometry of the volcanic arc (Völker et al., 2011), and the geochemistry of the eruptive products from these centers (López-Escobar et al., 1993). These segments are from north to south: the Northern (NSVZ), Transitional (TSVZ), Central (CSVZ), and Southern SVZ (SSVZ). The southernmost sector of the SSVZ consists of five major centers (Melimoyu, Mentolat, Macá, Cay, and Hudson) and numerous small monogenic eruptive centers (MEC) located along the Liquiñe-Ofqui Fault Zone (LOFZ; Fig. 1) and surrounding Hudson, Macá, and Cay (D'Orazio et al., 2003; Gutiérrez et al., 2005; Lahsen et al., 1997, 1994; López-Escobar et al., 1995a; Vargas et al., 2013). The LOFZ is a 1000-km-long major arc-parallel tectonic lineament that cuts through portions of the North Patagonian Batholith and is generated by the impingement of the Chile Rise against the continental margin and the oblique subduction of the Nazca Plate (Cembrano et al., 1996).

Based on the geochemistry of the basaltic lavas from the SSVZ centers, López-Escobar et al. (1993) generated a two-part classification based on the K₂O and Al₂O₃ contents and the relative abundance of incompatible elements such as high-field-strength elements (HFSE; Ti, Zr, Nb, Hf, U), large-ion lithophile elements (LILE; Cs, Rb, Ba, Sr, Th), and rare earth elements (REE). Among the volcanoes of the

southernmost SSVZ, Hudson and Melimoyu produce lavas and tephtras with relatively high concentrations of K₂O, HFSE, LILE, and REE and lower Al₂O₃ contents which correspond to the Type-II classification of López-Escobar et al. (1993) and have also been termed High Abundance (HA) geochemical centers (Fig. 4; Stern et al., 2015; Weller et al., 2017, 2015). The Type-1 geochemical classification of López-Escobar et al. (1993) are basaltic lavas with relatively low concentrations of K₂O, HFSE, LILE, and REE and higher Al₂O₃ contents that have also been termed Low Abundance (LA) geochemical centers. Among the volcanoes of the southern SSVZ, Macá, Cay, Mentolat and many of the MEC are Type-1 or LA geochemical centers. However, compared to Cay and Macá, Mentolat has produced lavas and tephtra with exceptionally low concentrations of K₂O, HFSE, LILE, and REE and has been further separated from the Type-I or LA classification and termed a Very Low Abundance (VLA) geochemical center (Fig. 4; Stern et al., 2016, 2015; Weller et al., 2017, 2015). Another distinctive feature of Mentolat-derived tephtras is the relatively high proportion of amphibole phenocryst that are absent or rare in the eruptive products from the other southernmost SSVZ centers (López-Escobar et al., 1993; Weller et al., 2017, 2015). The geochemical characteristics of Mentolat are similar to a few other volcanoes that also produce amphibole-bearing VLA-type eruptive products located further north in the Andean SVZ such as Nevado de Longaví (Rodríguez et al., 2007; Sellés et al., 2004), Calbuco (Hickey-Vargas et al., 1995; López-Escobar et al., 1995b), and Huequi (López-Escobar et al., 1993; Watt et al., 2011a).

Previous tephrochronologic studies from the region identified evidence for numerous small and large explosive eruptions, preserved as tephtras, derived from the southernmost volcanoes of the SSVZ. These studies utilized the tephtra geochemistry, as well as petrographic features such as glass color and vesicle abundance and morphology and the type and abundance of mineral phases, to identify potential source volcanoes for tephtras identified both in proximal outcrops (Naranjo and Stern, 1998, 2004) and more distal lacustrine sedimentary cores and

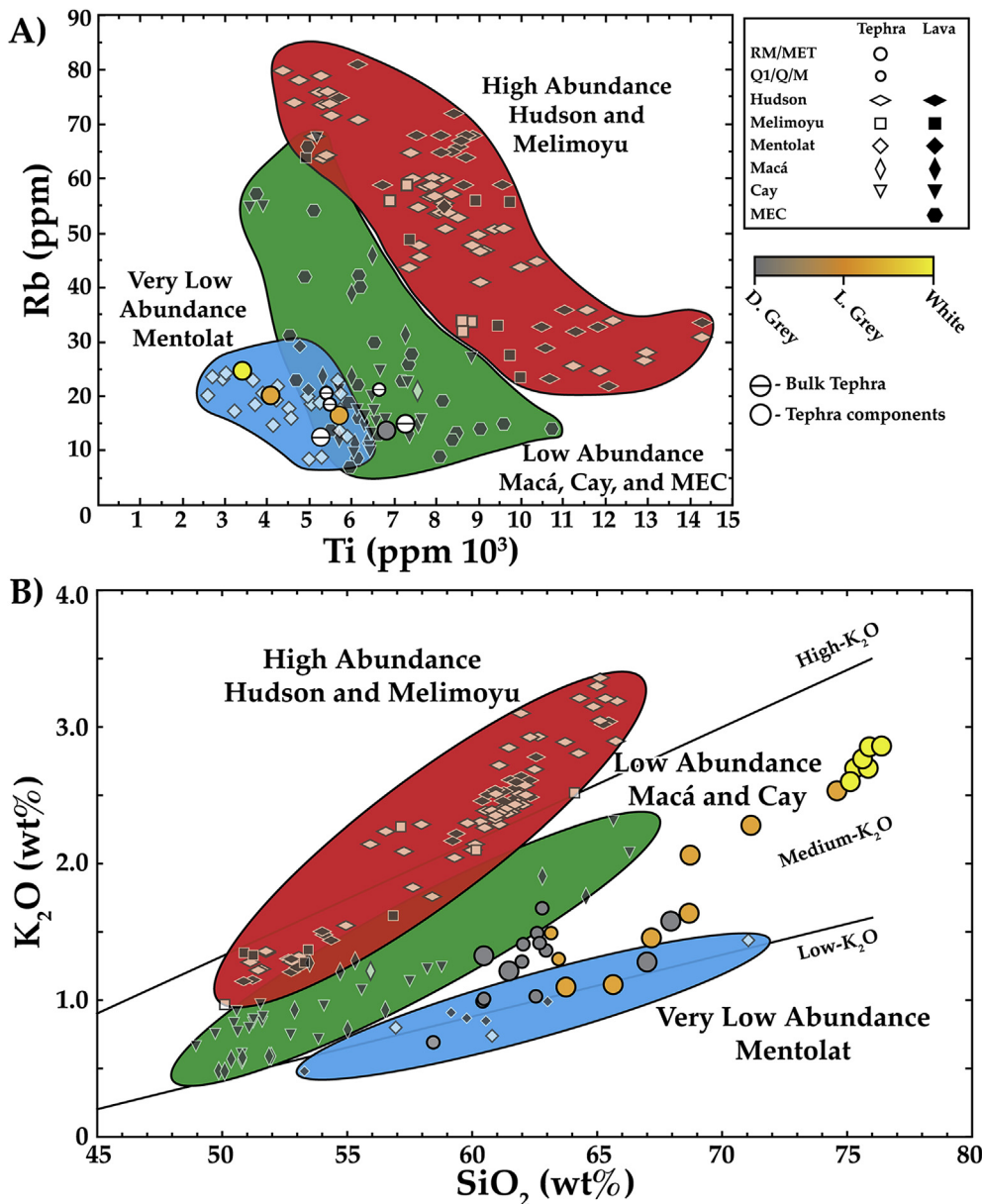


Fig. 4. A. Ti versus Rb in parts-per-million (ppm) illustrating the compositional fields for lavas (closed symbols) and bulk tephra (open symbols) for centers of the southernmost SSVZ and the monogenetic eruptive centers (MEC). The eruptive products of Hudson and Melimoyu are both High Abundance centers that have higher Ti and Rb contents than Macá, Cay or Mentolat. Macá, Cay and the MEC are all Low Abundance (LA) centers. The eruptive products from the Very Low Abundance (VLA) Mentolat volcano have generally lower Ti and Rb content than the Low Abundance (LA) Macá, Cay and the MEC centers. The glass (open circles color coded to the pumice color) and bulk tephra compositions (open circles with horizontal line) of the RM outcrop and MET core tephra have similar Ti and Rb contents as tephra Q1 from lake cores near Coyhaique (Weller et al., 2015) and tephra Q and M from the Río Cisnes valley (Stern et al., 2015; Weller et al., 2017). B. SiO₂ versus K₂O contents (wt. %) for published whole rock (closed symbols) and tephra glass (open symbols) from Melimoyu, Hudson, Macá, Cay and Mentolat illustrating the separation into the High Abundance (HA), Low Abundance (LA), and Very Low Abundance (VLA) compositional fields. The glass compositions of the RM outcrop (large color coded circles) and glass compositions of tephra Q1 (small color coded circles) observed in lake cores near Coyhaique (Weller et al., 2015), are low to medium-K₂O calc-alkaline compositions. The published geochemical data are those of D’Orazio et al. (2003), Futa and Stern (1988), Gutiérrez et al. (2005), Kratzmann et al. (2010, 2009), López-Escobar et al. (1995, 1993), Naranjo and Stern (2004, 1998), Stern et al. (2015, 2016), Weller et al. (2014). Geochemical classification division lines are from Ewart (1982). (For interpretation of the references to color in this figure legend, the reader is referred to the Web version of this article.)

subaerial exposures located to the southwest (Haberle and Lumley, 1998), south and southeast near the towns of Coyhaique (Fig. 1; Weller et al., 2014, 2015) and Cochrane (Fagel et al., 2017; Stern et al., 2016), near Lago Buenos Aires (Bendle et al., 2017) and north in the Río Cisnes valley (Stern et al., 2015; Weller et al., 2017).

These studies attributed seven tephra deposits to small or medium-sized eruptions from Melimoyu, including the ~1680 cal years BP MEL2 and the 2765 cal years BP MEL1 eruptions (Naranjo and Stern, 2004; Stern et al., 2015; Weller et al., 2017). Eighteen tephra are attributed to small to medium eruptions from Mentolat, including the ~7700 cal years BP MEN1 eruption (Naranjo and Stern, 2004; Stern et al., 2016, 2015, Weller et al., 2017, 2015). The medium-sized MAC1 eruption at ~1440 cal years BP is attributed to Macá (Naranjo and Stern, 2004) and 17 other tephra may have been derived from either Macá, Cay or one of the numerous monogenetic eruptive centers (MEC; Weller et al., 2017, 2015) located along the LOFZ or surrounding the major centers. Four large explosive eruptions from Hudson include the very large late-glacial Ho event dated at between 17,380 and 18,460 cal years BP (Bendle et al., 2017; Van Daele et al., 2016; Weller et al., 2014), two other mid-Holocene eruptions, the H1 and H2 events

(Naranjo and Stern, 1998) that occurred at ~7500 cal years BP (Stern and Weller, 2012) and ~3865 cal years BP respectively, as well as the more recent 1991 AD eruption (Kratzmann et al., 2009; Naranjo et al., 1993) and > 30 other tephra attributed to smaller eruptions of Hudson since late-glacial time (Weller et al., 2015).

The volcanoes of the southernmost SSVZ are situated along a portion of the Northern Patagonian Batholith composed primarily of biotite and hornblende-granodiorites and tonalites that range in age from Early Cretaceous to Late Miocene (D’Orazio et al., 2003; Gutiérrez et al., 2005; Hervé et al., 1995, 1993; Pankhurst et al., 1999). Portions of these plutons spatially associated with the LOFZ are known to be deformed and foliated (Pankhurst et al., 1999).

2. Methods

This study presents information concerning two ~13 cm thick tephra deposits, one observed in a lacustrine sediment core taken from the small, internally drained Mallín el Toqui (MET) peat bog (−45.018535°, −71.959487°) and the other as a subaerial exposure located ~10 km to the west in the Río Maniguales (RM) valley

(-45.006567° , -72.145164°). The approximately 6.5 m core from the MET peat bog was taken using a modified Livingston piston corer (Wright, 1967). Transmitted x-ray images were taken of the cores to help in identification of the denser tephra deposits (Fig. 2) that appear as white layers compared to the less dense organic matter-rich sediments, which appears as the dark material the tephra are preserved within.

The tephra deposits were removed from the sediment core and the outcrop with a knife and washed in water to remove the clay fraction and organic matter. A portion of the deposit was examined using a petrographic microscope to identify features such as tephra glass color and morphology, as well as to determine the abundance and identity of mineral phases. Material including pumice, mineral phenocrysts, and distinctive crustal xenoliths were hand-picked from these deposits. A portion of those components were mounted on petrographic slides and polished. The other material was prepared for trace element and isotopic analysis. Trace element contents of the samples were determined using two techniques. For the first technique, samples were powdered using a quartz pestle and mortar and digested in a mixture of HCl, HF, and HClO₄ for trace element analysis using a Thermo Finnigan Element2 sector field inductively-coupled plasma mass spectrometer (ICP-MS). Another portion of the deposit was powdered in a molybdenum shatter box, dissolved in a mixture of HF and HNO₃ for trace element analysis using an ELAN D CR ICP-MS. At the concentration level within these tephra, trace-element compositions are accurate within $\pm 10\%$ based on repeat analyses of internal and external standards with known compositions (Saadat and Stern, 2011).

Major element glass compositions of the pumice lapilli and mineral phenocrysts were measured at the University of Colorado at Boulder using a Jeol JXA-733 Electron Microprobe that was operating at 15 KV accelerating potential with a 5 nA probe current for the glasses and 15 KV and 20 nA current for the mineral phases. Glass compositions are normalized to 100% nominally anhydrous basis. Amphibole phenocrysts were measured on a Jeol JXA-8230 operating at 15 KV accelerating potential and 20 nA current. A defocused beam was used to obtain the analysis on the glasses and amphibole phenocrysts.

Strontium isotopic ratios were measured on a Finnigan-Mat 261 four-collector static Thermal Ionization Mass Spectrometer. In open containers, the powdered samples were dissolved in HF and HClO₄. Based on replicate analysis of the SRM-987 standard yielded a mean $^{87}\text{Sr}/^{86}\text{Sr}$ of $0.71025 \pm 2 (2\sigma)$ and the $^{87}\text{Sr}/^{86}\text{Sr}$ were corrected to SRM-987 = 0.710299 ± 8 . Errors of the 2σ refer to the last two digits of the $^{87}\text{Sr}/^{86}\text{Sr}$ ratio. Further details of the analytical procedure are outlined in Farmer et al. (1991).

AMS radiocarbon ages determined by DirectAMS Radiocarbon Dating Services (Brothwell, Washington, USA) on organic matter in the MET sediment core were converted to calendar years before present (cal years BP) by applying the ShCal13 curve (Hogg et al., 2013) to the CALIB 7.0.4 program (Stuiver et al., 1998).

3. Results

Included in the results are the lithostratigraphic information for the two tephra deposits studied and for other correlative tephra identified in lacustrine sediment cores from the Río Cisnes valley and from near Coyhaique (Table 1; Stern et al., 2015; Weller et al., 2018, 2017, 2015), tephra glass major and trace element compositions (Fig. 4; Tables 2 and 3), tephra strontium isotope ratios (Fig. 5; Table 4), amphibole compositions and thermobarometric estimates (Figs. 6–8; Tables 5 and 6, and S1 of the supplementary material), compositions of the plagioclase, pyroxenes, olivine, and minerals in the crustal xenoliths (Fig. 7; Table 7 and S2–S4 of the supplementary material), and the new radiocarbon age determinations from the MET sediment core (Fig. 2; Table 8).

3.1. Tephra components

Both tephra contain pumice lapilli with a diversity of colors and morphologies. These different components include a small proportion of black scoria, dark grey pumice with abundant plagioclase microlites, and a larger proportion of vesicle-rich light grey and white pumice lapilli with abundant phenocryst of plagioclase and amphibole. In both tephra the white pumice occurs in greater abundance near the base of the deposit (Fig. 3), but otherwise the different tephra components are randomly mixed within the deposits and show no other distinct vertical stratification within either the MET lake core or RM outcrop. These tephra also contain separated and fragmented crystals of plagioclase, amphibole, orthopyroxene and clinopyroxene, and a small proportion of Fe-Ti oxides and olivine, as well as a minor proportion of distinctive crustal xenoliths that range in texture from unfoliated to foliated and consist of pale green amphibole, Na-rich plagioclase, biotite, Fe-Ti oxides, and minor titanite (Fig. 9; Table 5, S1, S2, and S4).

On the basis of their color, a dark grey, light grey and white group of pumice were selected for major and trace element analysis. Crustal xenoliths were also hand-picked and powdered together for trace and isotopic analysis. Glass major element contents of the selected pumice components range from 59 up to 76 wt. % SiO₂ and are low-to medium-K₂O calc-alkaline volcanic products which plot between the compositional fields defined by previous published analysis of lava and glasses from Mentolat (López-Escobar et al., 1993; Stern et al., 2016), Macá and Cay (D'Orazio et al., 2003; Futa and Stern, 1988; López-Escobar et al., 1993; Naranjo and Stern, 2004). The different colored pumice components span nearly the entire range of glass compositions with the white pumice occupying a narrow interval at higher silica contents, while the dark grey and grey pumice groups overlap in their compositions. The glass composition are similar to glasses from tephra Q1, which has a similar age, collected from lake cores near the town of Coyhaique (Fig. 4, Tables 1–3; Weller et al., 2018, 2015). The trace element contents of the dark grey, light grey, and white pumice lapilli are consistent with the dark grey pumice being the most mafic component having higher concentrations of Sr, Ti, Mn, Sc, V, Cr, Co, Ni and lower concentrations of Rb, Ba, Zr, and Nb than either the light grey or white pumice (Table 3). The trace element contents of these tephra are similar to the bulk trace element contents of tephra Q of a sediment core from Laguna Las Mellizas (LLM in Fig. 1; Table 1), tephra M in a sediment core from Lake Shaman (LS in Fig. 1) in the Río Cisnes valley (Stern et al., 2015; Weller et al., 2017), and tephra Q1 from lake cores from near Coyhaique (Weller et al., 2015). The trace element contents of the selected components fall within the compositional field for both lavas and tephra derived from the southernmost SSVZ centers (Fig. 4B) with the white and light grey pumice components plotting within the compositional field for previous published analysis of Mentolat eruptive products, while the darker, more mafic components fall within the compositional fields of Macá, Cay and the MEC (Fig. 4A).

The Sr isotopic ratios (Table 4) of the white pumice from the RM outcrop deposit ($^{87}\text{Sr}/^{86}\text{Sr} = 0.704174 \pm 12$) and the bulk tephra Q from Laguna Las Mellizas ($^{87}\text{Sr}/^{86}\text{Sr} = 0.704171 \pm 9$) are similar to each other and to the eruptive products of a number of volcanoes of the southernmost SSVZ, including Mentolat (Fig. 5), but clearly lower than those for samples from Hudson volcano. The xenolith data, which represents numerous different grains selected from the tephra, have lower Sr isotope ratios ($^{87}\text{Sr}/^{86}\text{Sr} = 0.703928 \pm 9$) than any lavas or tephra from the SSVZ centers and also lower than isotopic ratios measured from metabasalts located on Isla Magdalena where Mentolat is located (Fig. 5; Hervé et al., 1995, 1993).

3.2. Mineral chemistry

The analyzed minerals in the tephra occur as either phenocryst embedded within glass and others that have become dislodged from the glass and were hand-picked from the deposit. Amphibole phenocrysts

Table 2

Major element compositions (wt. % oxide) of selected components from the MET and RM tephtras and the correlated tephra Q1 (Weller et al., 2015) from cores near Coyhaique (Table 1).

Tephra	RM	RM	RM	RM	RM	RM	RM	RM	RM						
Material	Glass	Glass	Glass	Glass	Glass	Glass	Glass	Glass	Glass						
Color	White	White	White	White	White	White	L. Grey	D. Grey	D. Grey						
Location	RMV	RMV	RMV	RMV	RMV	RMV	RMV	RMV	RMV						
SiO ₂	75.12	75.33	76.38	75.89	75.84	75.60	74.59	68.72	67.20	63.75	68.67	65.64	71.15	67.00	67.94
TiO ₂	0.23	0.13	0.11	0.09	0.13	0.08	0.16	0.74	0.40	0.36	0.30	0.22	0.40	0.42	0.49
Al ₂ O ₃	14.11	14.49	13.53	13.67	14.10	14.14	14.08	12.47	17.37	13.49	17.00	20.21	13.06	18.89	17.71
FeO	1.32	1.19	1.31	1.32	1.44	1.23	1.67	5.97	2.86	7.20	2.72	1.77	4.17	1.55	1.44
MnO	0.00	0.14	0.02	0.19	0.00	0.14	0.21	0.41	0.00	0.37	0.00	0.02	0.35	0.02	0.12
MgO	0.18	0.12	0.15	0.14	0.14	0.12	0.21	1.93	0.64	5.41	0.86	0.35	1.30	0.15	0.13
CaO	1.12	0.92	0.84	1.02	1.02	0.95	1.29	2.59	4.10	4.18	3.11	4.79	2.00	4.32	3.76
Na ₂ O	5.30	4.82	4.79	4.81	4.64	4.98	5.25	4.44	5.65	3.94	5.66	5.69	5.17	5.93	6.29
K ₂ O	2.61	2.70	2.86	2.86	2.70	2.77	2.54	2.07	1.46	1.10	1.64	1.11	2.27	1.28	1.58
P ₂ O ₅	0.00	0.16	0.02	0.00	0.00	0.00	0.00	0.65	0.31	0.20	0.04	0.20	0.13	0.45	0.55
Total	100	100	100	100	100	100	100	100	100	100	100	100	100	100	100

Tephra	RM	RM	RM	^a Q1											
Material	Glass	Glass	Glass	Glass	Glass	Glass	Glass	Glass	Glass	Glass	Glass	Glass	Glass	Glass	Glass
Color	D. Grey	D. Grey	D. Grey	L. Grey	L. Grey	D. Grey									
Location	RMV	RMV	RMV	LTr											
SiO ₂	63.43	61.47	60.47	63.44	63.19	62.08	62.54	62.78	62.94	62.72	62.69	61.98	60.43	60.43	58.41
TiO ₂	1.64	0.77	1.28	1.19	1.13	1.31	1.06	1.29	1.01	1.20	1.45	1.06	0.84	0.90	0.76
Al ₂ O ₃	13.34	17.74	17.58	16.61	16.34	16.60	16.24	15.29	16.32	16.22	14.35	17.48	18.03	17.80	18.63
FeO	8.52	5.76	6.63	6.12	6.57	6.41	5.55	7.02	6.54	6.69	8.14	5.75	6.29	5.99	6.26
MnO	0.16	0.00	0.00	0.00	0.25	0.16	0.18	0.02	0.32	0.12	0.07	0.19	0.25	0.20	0.25
MgO	1.22	2.04	1.22	1.41	1.84	1.95	2.36	1.94	1.70	1.99	2.73	1.50	1.85	2.19	2.84
CaO	3.86	5.28	5.30	4.27	4.22	4.34	5.33	3.95	4.18	4.23	4.04	5.11	5.85	5.86	6.69
Na ₂ O	4.92	5.44	5.79	5.32	4.74	5.41	5.45	5.60	5.42	5.03	4.86	5.38	5.04	5.37	5.27
K ₂ O	2.36	1.21	1.32	1.30	1.49	1.41	1.02	1.67	1.37	1.49	1.42	1.28	0.99	1.01	0.69
P ₂ O ₅	0.55	0.29	0.42	0.34	0.22	0.33	0.26	0.43	0.20	0.30	0.25	0.27	0.44	0.24	0.19
Total	100	100	100	100	100	100	100	100	100	100	100	100	100	100	100

RMV-Río Maniguales valley.

^a Weller et al. (2015).

are an abundant phase and occur as euhedral to subhedral grains that are dark brown in color and lack oxidation rims. The amphibole phenocrysts are present in all the different colored pumice lapilli indicating amphibole stability in the entire chemical range of erupted material. Table 5 presents representative analyses of amphiboles from the MET and RM tephtras, and other samples from Mentolat, Melimoyu and Cay volcanoes. All of the amphibole geochemical data are included in Table S1.

Amphiboles from Mentolat-derived tephtras are embedded within the pumice or they occur as loose phenocrysts that were hand-picked from tephtras B2, D1, Q3, and MENO observed in lacustrine sediment cores near Coyhaique (Weller et al., 2015), and tephra I from the Río Cisnes valley (Weller et al., 2017). The amphibole phenocrysts from Mentolat are large euhedral to subhedral grains that are dark brown in color, show no core to rim variation, and lack oxidation rims. Amphiboles from Cay volcano were analyzed from samples of a volcanic plug near the summit that is dacitic in composition (Futa and Stern, 1988) and contains phenocrysts of plagioclase, orthopyroxene, amphibole, and Fe-Ti oxides (Fig. 10). These amphiboles occur as small subhedral to euhedral grains that are brown in color and commonly have fine-grained opacitic oxidation rims (Fig. 10). The amphiboles analyzed from Melimoyu occur in rhyolitic pumice from the MEL1 and MEL2 eruptions (Naranjo and Stern, 2004). They are euhedral to subhedral and range from dark green to brown and do not have oxidation rims.

Geochemically, amphiboles from the MET and RM tephtras range in K₂O from 0.20 to 0.37 wt. % and TiO₂ from 1.5 to 3.8 wt. % (Fig. 6) and are similar to the Mentolat derived phenocryst that range in K₂O from

0.14 to 0.43 wt. % and TiO₂ from 1.9 to 2.4 wt. % (Fig. 6; Table 5 and S1). Amphiboles from Melimoyu have higher K₂O (0.39–0.52 wt. %) and TiO₂ (2.8–4.5 wt. %) while the amphiboles from Cay have similar TiO₂ (2.4–3.1 wt. %) but higher K₂O (0.47–0.55 wt. %; Fig. 6, Table 5 and S1). Amphiboles from the crustal xenoliths in the MET and RM tephtras are pale green in color and have much lower TiO₂ content < 0.51 wt. % and a much wider range of K₂O contents (0.13–0.9 wt. %) than any amphiboles from the southernmost SSVZ centers (Figs. 6 and 7).

Thermobarometric formulations of Ridolfi et al. (2010) are used to estimate the conditions during the formation of amphibole phenocrysts (Fig. 8, Table 6 and S1), which are utilized as a tool to distinguish between the amphiboles derived from the SSVZ centers and to identify a potential source volcano for the MET core and RM outcrop tephtras. The amphiboles in the MET core and RM outcrop tephtras formed over a wide range of temperatures (834–969 °C), pressures (154–406 MPa), and host magma H₂O water contents (4.9–7.0 wt. %) with oxygen fugacity slightly below the NNO + 1 buffer (Nickel-Nickel oxide; Fig. 8; Table 6). Amphiboles from the other Mentolat-derived tephtras formed over a similar range of pressures (128–579 MPa), temperatures (832–1014 °C), and host magma water contents (4.4–7.8 wt. %). The amphiboles from Melimoyu and Cay formed over a more restricted range of conditions with temperature estimates from 898 to 967 °C for Melimoyu and 870–917 °C for Cay, pressures of 198–376 for Melimoyu and 193–264 MPa for Cay, and host melt water contents of 4.1–5.8 wt. % at Melimoyu and 5.1–5.6 wt. % at Cay (Fig. 8, Table 6 and S1).

The MET core and RM outcrop tephtras also contains abundant

Table 3

Trace element in parts-per-million (ppm) of selected MET and RM tephra components and for other correlated tephras.

Sample	RM	RM	RM	RM	MET	MET	^a Q	^b Q1	^c M	RM
Location	RMV	RMV	RMV	RMV	Mallín el Toqui	Mallín el Toqui	LLM	–	LS	RMV
Lab ID	DJW-19	DJW-20b	DJW-21	DJW-18	CS0017	CS0018	DJW-60	Avg.	CS5063	DJW-57
Material	Pumice	Pumice	Pumice	Bulk	Bulk	Pumice	Bulk	Bulk	Bulk	Xenoliths
Color	White	L. Grey	D. Grey	–	–	L. Grey	–	n = 3	–	–
Sc	10.1	13.4	22.7	24.5	–	–	21.3	–	–	26.9
Ti	<i>3408</i>	<i>4082</i>	<i>6820</i>	<i>7265</i>	<i>5265</i>	<i>5699</i>	<i>6639</i>	<i>5478</i>	<i>5380</i>	<i>9185</i>
V	<i>88</i>	<i>94</i>	<i>183</i>	<i>193</i>	<i>153</i>	<i>141</i>	<i>144</i>	<i>190</i>	–	<i>201</i>
Cr	<i>3</i>	<i>2</i>	<i>26</i>	<i>14</i>	<i>5</i>	<i>2</i>	<i>7</i>	<i>16</i>	–	<i>80</i>
Mn	<i>1136</i>	<i>1213</i>	<i>1279</i>	<i>1766</i>	<i>1359</i>	<i>1402</i>	<i>1153</i>	<i>1092</i>	<i>956</i>	<i>1204</i>
Co	<i>13</i>	<i>17</i>	<i>38</i>	<i>27</i>	<i>17</i>	<i>16</i>	<i>15</i>	<i>27</i>	–	<i>26</i>
Ni	<i>10</i>	<i>17</i>	<i>23</i>	<i>15</i>	<i>17</i>	<i>13</i>	<i>3</i>	<i>34</i>	–	<i>29</i>
Cu	<i>14</i>	<i>18</i>	<i>22</i>	<i>115</i>	<i>16</i>	<i>13</i>	<i>49</i>	<i>120</i>	–	<i>11</i>
Zn	<i>78</i>	<i>90</i>	<i>127</i>	<i>150</i>	<i>121</i>	<i>122</i>	<i>92</i>	<i>117</i>	–	<i>215</i>
Rb	<i>25</i>	<i>20</i>	<i>14</i>	<i>15</i>	<i>13</i>	<i>17</i>	<i>21</i>	<i>19</i>	<i>21</i>	<i>17</i>
Sr	<i>396</i>	<i>472</i>	<i>518</i>	<i>442</i>	<i>625</i>	<i>573</i>	<i>448</i>	<i>409</i>	<i>418</i>	<i>436</i>
Y	<i>20</i>	<i>22</i>	<i>26</i>	<i>29</i>	<i>21</i>	<i>25</i>	<i>29</i>	<i>22</i>	<i>17</i>	<i>28</i>
Zr	<i>122</i>	<i>98</i>	<i>92</i>	<i>66</i>	<i>64</i>	<i>97</i>	<i>158</i>	<i>104</i>	<i>79</i>	<i>16</i>
Nb	<i>5.7</i>	<i>4.0</i>	<i>3.2</i>	<i>4.7</i>	<i>DL</i>	<i>DL</i>	<i>4.4</i>	<i>4</i>	<i>4</i>	<i>10.3</i>
Cs	<i>1.0</i>	<i>0.5</i>	<i>0.8</i>	<i>0.4</i>	<i>1.6</i>	<i>1.2</i>	<i>1.0</i>	<i>0.9</i>	<i>0.8</i>	<i>0.9</i>
Ba	<i>329</i>	<i>239</i>	<i>271</i>	<i>198</i>	<i>238</i>	<i>258</i>	<i>322</i>	<i>231</i>	<i>267</i>	<i>180</i>
La	<i>13.53</i>	<i>14.05</i>	<i>13.54</i>	<i>13.51</i>	<i>10.4</i>	<i>11.65</i>	<i>13.20</i>	<i>11.07</i>	<i>10.5</i>	<i>14.50</i>
Ce	<i>33.24</i>	<i>35.62</i>	<i>32.81</i>	<i>33.61</i>	<i>25.9</i>	<i>28.46</i>	<i>32.82</i>	<i>25.55</i>	<i>24.0</i>	<i>40.27</i>
Pr	<i>4.13</i>	<i>5.10</i>	<i>4.59</i>	<i>4.60</i>	<i>3.5</i>	<i>3.98</i>	<i>4.28</i>	<i>3.47</i>	<i>3.9</i>	<i>4.90</i>
Nd	<i>17.37</i>	<i>22.34</i>	<i>19.08</i>	<i>20.10</i>	<i>16.3</i>	<i>19.05</i>	<i>18.45</i>	<i>16.00</i>	<i>16.3</i>	<i>20.08</i>
Sm	<i>4.37</i>	<i>5.63</i>	<i>4.96</i>	<i>5.40</i>	<i>4.00</i>	<i>4.37</i>	<i>4.54</i>	<i>3.77</i>	<i>3.43</i>	<i>5.03</i>
Eu	<i>1.44</i>	<i>1.99</i>	<i>1.71</i>	<i>1.79</i>	<i>1.63</i>	<i>1.60</i>	<i>1.53</i>	<i>1.21</i>	<i>1.10</i>	<i>1.75</i>
Gd	<i>4.07</i>	<i>5.93</i>	<i>5.39</i>	<i>5.93</i>	<i>5.0</i>	<i>5.42</i>	<i>4.85</i>	<i>4.59</i>	<i>4.3</i>	<i>4.91</i>
Tb	<i>0.63</i>	<i>0.84</i>	<i>0.79</i>	<i>0.92</i>	<i>0.65</i>	<i>0.76</i>	<i>0.75</i>	<i>0.52</i>	<i>0.55</i>	<i>0.78</i>
Dy	<i>4.10</i>	<i>5.34</i>	<i>5.21</i>	<i>5.82</i>	<i>4.08</i>	<i>4.32</i>	<i>4.90</i>	<i>3.62</i>	<i>3.72</i>	<i>4.55</i>
Ho	<i>0.80</i>	<i>1.09</i>	<i>1.03</i>	<i>1.15</i>	<i>0.75</i>	<i>0.87</i>	<i>0.99</i>	<i>0.67</i>	<i>0.58</i>	<i>0.92</i>
Er	<i>2.34</i>	<i>3.33</i>	<i>3.03</i>	<i>3.23</i>	<i>2.37</i>	<i>2.72</i>	<i>2.85</i>	<i>2.25</i>	<i>2.00</i>	<i>2.48</i>
Tm	<i>0.36</i>	<i>0.51</i>	<i>0.45</i>	<i>0.47</i>	<i>0.27</i>	<i>0.32</i>	<i>0.43</i>	<i>0.24</i>	<i>0.27</i>	<i>0.38</i>
Yb	<i>2.60</i>	<i>3.29</i>	<i>3.04</i>	<i>3.17</i>	<i>2.18</i>	<i>2.54</i>	<i>2.94</i>	<i>2.07</i>	<i>1.99</i>	<i>2.28</i>
Lu	<i>0.39</i>	<i>0.53</i>	<i>0.44</i>	<i>0.46</i>	<i>0.26</i>	<i>0.31</i>	<i>0.41</i>	<i>0.25</i>	<i>0.20</i>	<i>0.33</i>
Hf	<i>3.6</i>	<i>4.0</i>	<i>3.3</i>	<i>2.4</i>	<i>1.7</i>	<i>2.6</i>	<i>5.3</i>	<i>2.7</i>	<i>2.3</i>	<i>0.6</i>
Pb	<i>9.7</i>	<i>8.9</i>	<i>8.6</i>	<i>8.5</i>	<i>4.8</i>	<i>6.1</i>	<i>9.4</i>	<i>8.0</i>	<i>8.9</i>	<i>5.5</i>
Th	<i>4.6</i>	<i>2.9</i>	<i>3.2</i>	<i>2.5</i>	<i>0.6</i>	<i>0.8</i>	<i>3.7</i>	<i>1.8</i>	<i>2.1</i>	<i>2.0</i>
U	<i>1.0</i>	<i>0.7</i>	<i>0.8</i>	<i>0.7</i>	<i>0.3</i>	<i>0.4</i>	<i>0.9</i>	<i>0.5</i>	<i>0.6</i>	<i>0.3</i>

Letters in italics were measured on ELAN D CR ICP-MS.

RMV-Río Maniguales valley, DL-Detection limit.

^a Weller et al. (2017).^b Weller et al. (2015).^c Stern et al. (2015).

orthopyroxene and clinopyroxene and they occur as large euhedral grains with inclusions of apatite and Fe-Ti oxides. The clinopyroxene phenocryst occupy a narrow compositional range of En44-41, Wo45-40, Fs17-13 (Fig. 7A; Table 7 and S3) and the orthopyroxenes occupy a wider compositional range of En72-59, Wo3-2, Fs39-26 (Fig. 7A; Table 7 and S3). Olivine is a minor constituent in these tephras and it is observed as small subhedral grains within the dark grey pumice. The olivine phenocrysts occupy a narrow compositional range of Fo78-71 and Fa29-22 (Fig. 7A; Table 7 and S3).

Plagioclase is another abundant phenocryst phase in the MET core and RM outcrop tephras and they occur as large euhedral to subhedral grains and typically have complex zonation patterns and contain small inclusions of amphibole, apatite, Fe-Ti oxides, and pyroxenes. The plagioclase phenocryst range in An39-26, Ab72-59, Or2-1 and one core to rim pair show normal zonation pattern with the core composition having a higher An, and lower Ab and Or contents than the outer rim composition (Table 7 and S2). The plagioclase from the crustal xenoliths in these tephras are homogenous and show no core to rim variation and are slightly more evolved with a compositional range of An32-22, Ab78-67, Or < 1 (Fig. 7B; Table 7 and S2).

Titanite is only observed in the crustal xenoliths and it is commonly

found as small anhedral grains. They are commonly associated with Fe-Ti oxides. Geochemically, the titanite from the xenoliths are similar to titanite measured from xenoliths within lavas from Hudson volcano (Table S4; Gutiérrez et al., 2005).

3.3. Tephra correlation

A radiocarbon age determination done on the organic matter-rich lacustrine sediments directly above the ~13 cm tephra in section T10 of the MET sediment core constrains its age to $\geq 11,728$ cal years BP (10,109 ¹⁴C yr BP; Fig. 2; Table 8; Hogg et al., 2013; Stuiver et al., 1998). Tephra M of the upper Río Cisnes valley is constrained in age to 11,140 cal years BP by interpolating the age between stratigraphically older and younger radiocarbon age estimates and assuming a constant sedimentation rate (Stern et al., 2015). Tephra Q1 of Lake La Trapanda from near Coyhaique is constrained in age to 11,142 cal years BP that is estimated using a Bayesian statistical method (Weller et al., 2018). The age estimates for tephra Q1 observed in lake cores near Coyhaique and tephra M of the upper Río Cisnes valley are ~600 years younger than the radiocarbon age determination from just above the tephra in the MET sediment core (Fig. 2). Radiocarbon ages determined

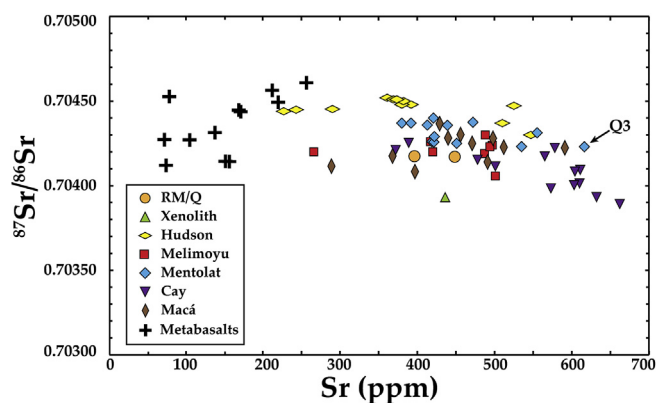


Fig. 5. $^{87}\text{Sr}/^{86}\text{Sr}$ vs Sr content in part-per-million (ppm) for the volcanic products of the Southernmost SSVZ centers. The Sr isotopic ratios for the white pumice from the RM tephra, and for bulk tephra Q of the Río Cisnes valley (Weller et al., 2017) which are similar to each other, fall within the range for both lavas and tephra from Mentolat and other SSVZ centers including Melimoyu, Macá, and Cay (D'Orazio et al., 2003; Futa and Stern, 1988; Notsu et al., 1987; Weller et al., 2017) but clearly lower than the eruptive products from Hudson (Futa and Stern, 1988; Naranjo and Stern, 1998; Notsu et al., 1987; Stern, 2008; Weller et al., 2014). Also shown are the isotopic composition of the crustal xenolith, which have higher Sr contents but lower Sr isotope ratios than metabasalts from the Isla Magdalena region (Hervé et al., 1995, 1993).

on bulk sediments have been shown to be older than their true age due to the input and deposition of older organic matter into the lacustrine system (Bertrand et al., 2012). Age discrepancies of this magnitude can be expected for radiocarbon age determinations of bulk lacustrine sediments.

The MET and RM tephra share similar tephra geochemistry (Fig. 4), petrography, and have similar ages as other tephra previously described from the region including the amphibole-bearing tephra Q and tephra M from the lower and upper Río Cisnes valley respectively (Table 1; Stern et al., 2015; Weller et al., 2017), and also tephra Q1 from multiple lake sediment cores near Coyhaique (Table 1; Weller et al., 2018, 2015). Thus, these likely correspond to the same eruptive event and we correlate the MET and RM tephra with these other deposits previously described from the region which will be termed the ~11.7 ka MEN tephra.

The tephra are ~13 cm thick deposits in both the MET sediment core (Fig. 2) and the RM tephra outcrop (Fig. 3; Table 1). In the MET core, the coarsest pumice grains occur at the base of the deposit and have a maximum diameter of 7.1 mm, while in the outcrop the maximum pumice diameter is 13.0 mm (Table 1) and there is less apparent grain size sorting. The maximum grain diameter of tephra Q and M of the lower and upper Río Cisnes valley respectively, are lower than those observed in the MET the RM outcrop tephra (Table 1) and the maximum grain size decreases with distance from Mentolat. Tephra Q1 of the lake cores from near Coyhaique (Fig. 1) also show a decrease in the maximum grain size diameter away from the RM and MET tephra sites. The tephra lithostratigraphic data indicate that the eruption plume and the locus of tephra deposition was likely located south of the Río Cisnes valley and north of the lake cores located near Coyhaique (Fig. 11) and

Table 4

Strontium isotopic ratios and the Sr content (ppm) for the RM tephra and other Mentolat-derived tephra from the region.

Tephra Name	Location	Material	$^{87}\text{Sr}/^{86}\text{Sr}$	Sr (ppm)	Lab #	Reference
RM	RMV	White Pumice	0.704174 ± 12	396	PC-3	This study
Q	LLM	Bulk	0.704171 ± 9	448	DJW-59	Weller et al. (2017)
Q3	LLT	Bulk	0.704229 ± 12	616	DJW-58	Weller et al. (2018)
RM	RMV	Xenoliths	0.703928 ± 9	436	PC-4	This study

RMV-Río Maniguales valley.

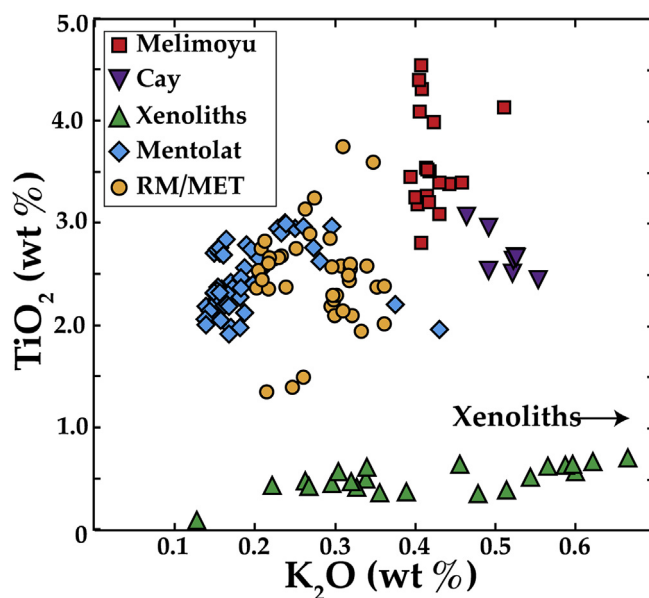


Fig. 6. K_2O versus TiO_2 (wt. %) of amphibole phenocrysts from the ~11.7 ka MEN tephra compared to amphiboles analyzed in other tephra derived from Mentolat and Melimoyu and lavas from Cay. The geochemistry of the amphibole phenocrysts from the ~11.7 ka MEN tephra occupy a wide compositional range and are most similar to Mentolat-derived amphiboles. The pale green amphiboles from the crustal xenoliths in the MET and RM tephra are clearly compositionally distinct (less 1 wt. % TiO_2) from any of the igneous amphiboles derived from the southernmost SSVZ centers. (For interpretation of the references to color in this figure legend, the reader is referred to the Web version of this article.)

that the eruptive material was dispersed predominately to the southeast reaching a thickness of ~13 cm 95 km from the source vent.

Using the tephra lithostratigraphic data, tephra isopachs of 10-, 2-, 1-, and 0.5-cm have been estimated for the ~11.7 ka MEN eruption (Fig. 11). It should be noted that the isopachs are conservative and loosely constrained, especially in the lacustrine sediment cores from near Coyhaique where subtle tephra thicknesses variations exist between the lake cores (Fig. 1) that may be related to modification by processes within the lacustrine system (Bertrand et al., 2014). Using these isopachs (Fig. 11), an estimated volume of ~1.8 km³ of erupted material was derived from this event. Assuming a bulk tephra density of 900 kg/m³, the eruption magnitude (Pyle, 2015) is estimated to be 5.2.

4. Discussion

The petrographic observations and geochemical characteristics of the MET and RM tephra, suggest that it was derived from Mentolat volcano. All of the previously analyzed lavas and tephra from Macá and Cay have LA-type geochemistry and at a given SiO_2 content, have higher concentrations of K_2O , HFSE, LILE, and REE, while Mentolat has produced lavas and tephra with VLA-type geochemistry and lower concentrations of K_2O , HFSE, LILE, and REE (Fig. 4). The glass major and trace element geochemistry of the MET sediment core and RM

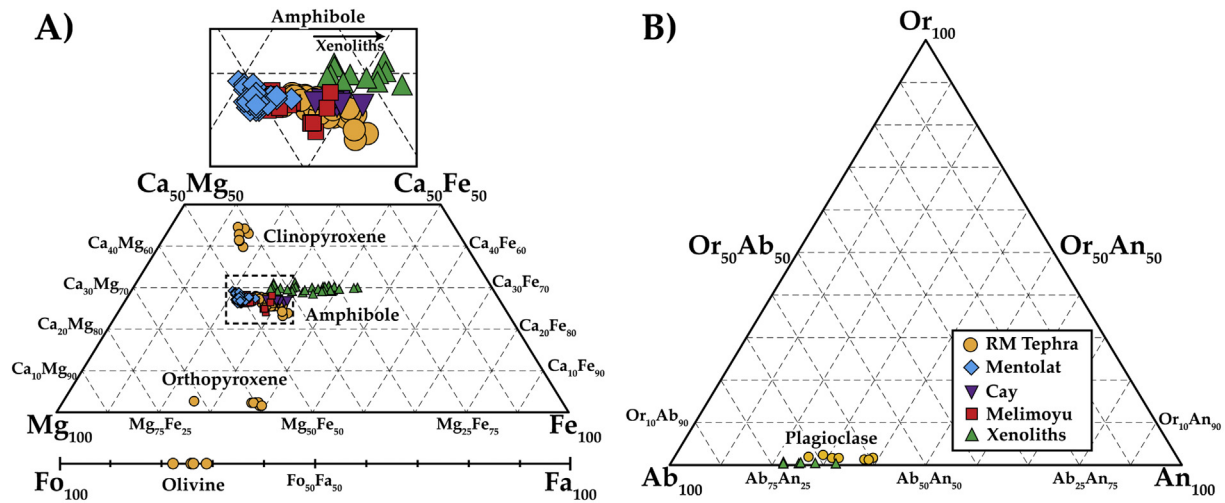


Fig. 7. A) Ca-Mg-Fe compositional classification diagrams for pyroxenes, amphiboles and olivines of the MET and RM tephtras, including the compositional classification of the amphibole phenocryst observed in tephtras derived from Mentolat and Melimoyu and in lavas from Cay. Clinopyroxenes are augites and orthopyroxenes are hypersthene. Small inset box shows amphibole compositions with the majority of the centers having overlapping compositions except the pale green amphiboles from the xenoliths with have a much wider range of Fe component. B) Or-Ab-An classification diagram for plagioclase from the ~11.7 ka MEN tephtra and the crustal xenoliths they contain. Plagioclase from the tephtras and the crustal xenoliths are both rich in the albite component, but the plagioclase crystals from the crustal xenoliths have lower orthoclase component compared to plagioclase phenocrysts and microlites in the RM outcrop tephtra. (For interpretation of the references to color in this figure legend, the reader is referred to the Web version of this article.)

outcrop tephtras have VLA-type character of both lavas and tephtra derived from Mentolat volcano (Fig. 4). The relative abundance of amphibole in these tephtras is consistent with the observations of other tephtras derived from Mentolat (Weller et al., 2017, 2015). The amphibole geochemistry (Fig. 6; Table 5) and thermobarometry (Fig. 8;

Table 6 and S1) estimates are most similar to amphiboles from the Mentolat-derived tephtras and are compositionally distinct from Melimoyu and Cay amphiboles (Fig. 6).

The tephtra glass and mineral chemistry of the MET and RM tephtras, supports Mentolat volcano as the likely source. Although the more

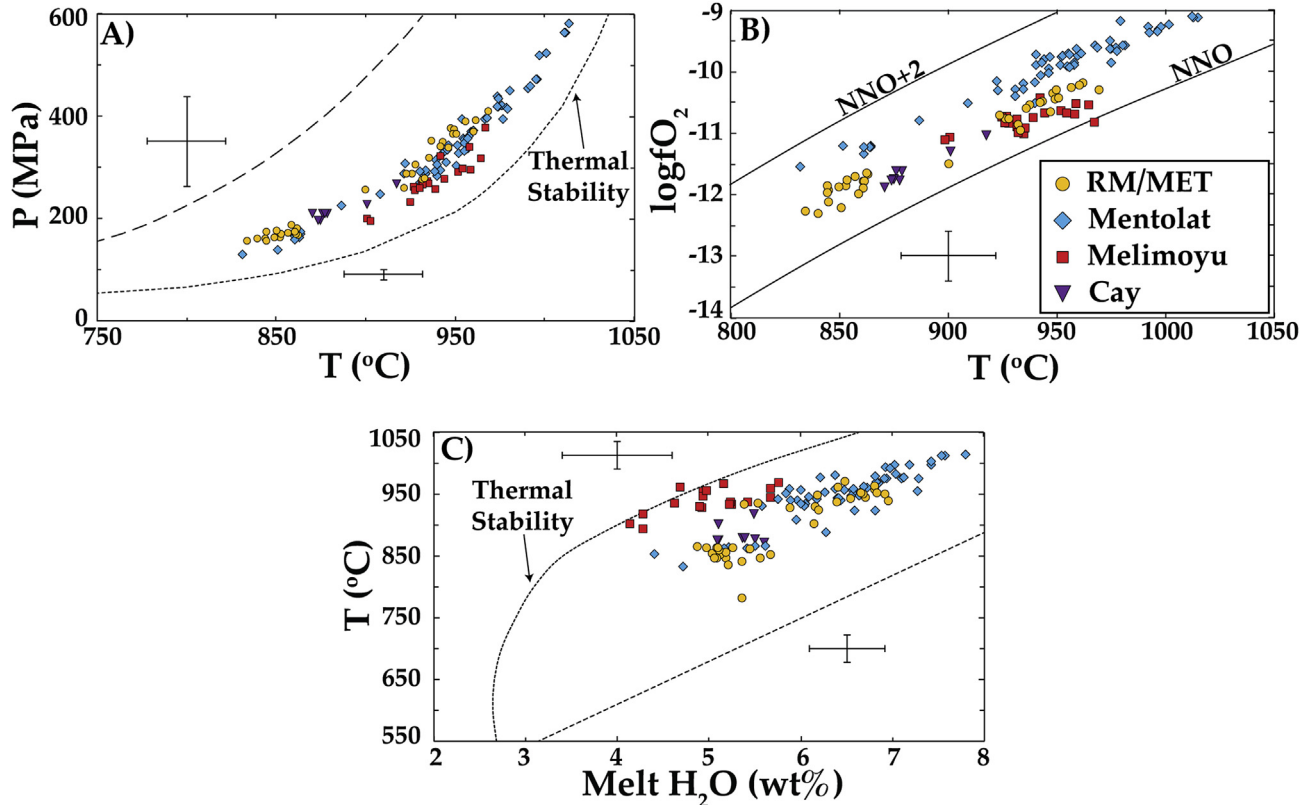


Fig. 8. Physicochemical conditions, calculated from the formulations of Ridolfi et al. (2010), during the formation of the amphiboles for lavas from Cay and tephtras from explosive eruptions of Melimoyu and Mentolat. The amphiboles from the MET and RM tephtras are formed over a wide range of temperatures, pressures, melt H₂O content (wt. %), and oxygen fugacity between the NNO (Nickel-Nickel oxide) and NNO + 1 buffer, and fall in a range of physical and chemical characteristics similar to amphiboles derived from other explosive eruptions from Mentolat (Weller et al., 2015, 2017).

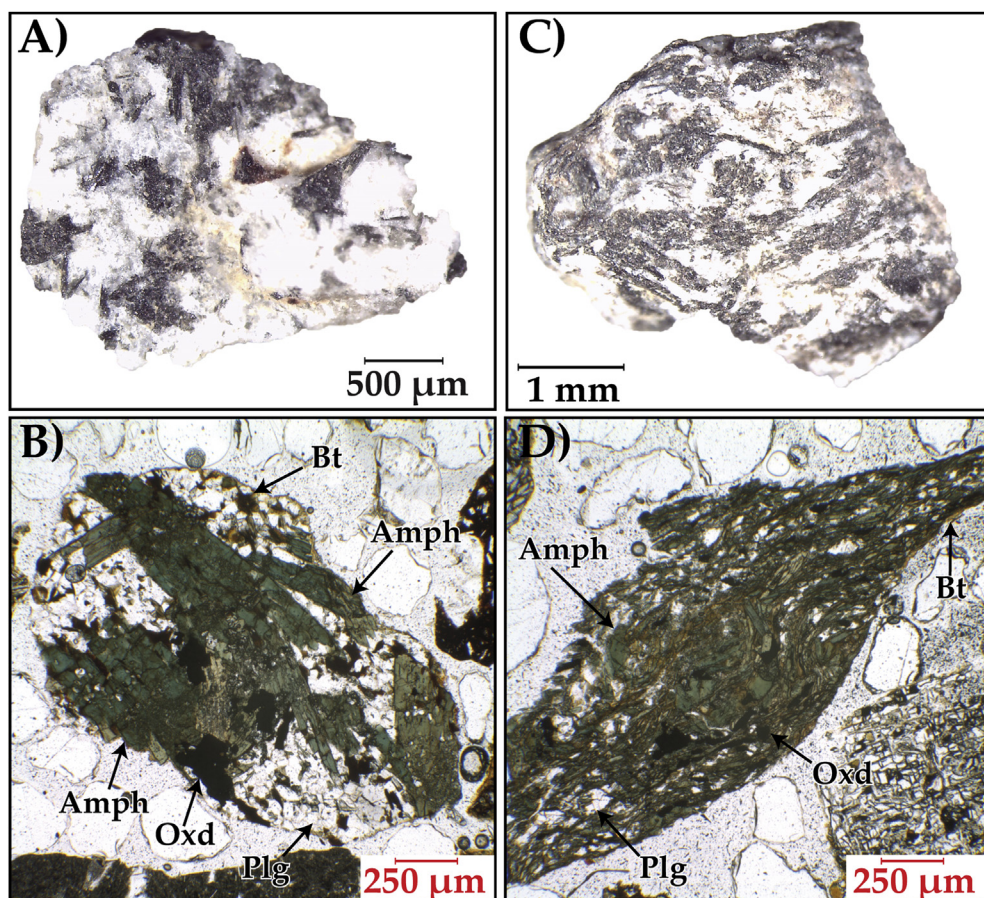


Fig. 9. Photographs and photomicrographs of crustal xenoliths within the MET sediment core and RM outcrop tephra deposits. These xenoliths have both unfoliated (A and B) and foliated metamorphic fabrics (C and D), all containing pale green amphibole, Na-plagioclase, biotite, Fe-Ti oxide and titanite. (For interpretation of the references to color in this figure legend, the reader is referred to the Web version of this article.)

Table 5

Representative electron microprobe analyses (wt. % oxide) of amphiboles from the MET and RM tephtras and from lavas and tephtras derived from Mentolat and other southernmost SSVZ centers.

Volcano	Tephra	Material	SiO ₂	TiO ₂	Al ₂ O ₃	FeO	MnO	MgO	CaO	Na ₂ O	K ₂ O	Cr ₂ O ₃	F	Cl	Total	Ca	Mg	Fe
Mentolat	RM, MET	Tephra	42.47	2.59	11.10	13.83	0.38	12.91	10.70	2.60	0.30	0.01	0.05	0.16	97.1	27.1	45.5	27.4
Mentolat	B2	Tephra	45.78	2.34	8.56	11.87	0.41	14.97	10.77	2.08	0.15	0.01	0.03	0.09	97.0	26.4	51.0	22.7
Mentolat	D1	Tephra	41.82	2.78	14.08	10.19	0.12	14.80	11.90	2.54	0.19	0.00	0.01	0.01	98.4	29.4	50.9	19.7
Mentolat	I	Tephra	42.69	2.12	11.61	12.34	0.31	14.16	11.32	2.42	0.19	0.02	0.00	0.04	97.2	27.9	48.5	23.7
Mentolat	Q3	Tephra	42.55	2.32	12.41	11.08	0.15	14.90	11.25	2.51	0.16	0.00	0.02	0.07	97.4	27.7	51.0	21.3
Mentolat	MENo	Tephra	41.91	2.36	12.79	11.14	0.14	14.39	11.31	2.65	0.18	0.00	0.02	0.01	96.9	28.3	50.0	21.7
Melimoyu	MEL1, MEL2	Tephra	42.19	4.35	11.05	11.89	0.29	13.59	10.84	2.73	0.41	0.02	0.04	0.24	97.6	27.8	48.4	23.8
Cay	C12	Lava	44.05	2.69	9.26	14.66	0.32	12.63	10.74	2.13	0.53	0.01	0.08	0.33	97.4	27.0	44.2	28.8
Mentolat	RM, MET	Xenolith	44.76	0.49	12.05	16.76	0.25	10.24	11.19	1.49	0.32	0.03	0.00	0.02	97.6	29.0	37.0	34.0

mafic glass compositions are similar to the previous published eruptive products from Mentolat, with increasing SiO₂ they form a distinct trend towards higher K₂O compared to other felsic compositions previously reported from this volcano (Fig. 4B; López-Escobar et al., 1993; Stern et al., 2016; Weller et al., 2017). Nevertheless, they do maintain their VLA character with respect to trace element concentrations (Fig. 4A). These results indicate that there is greater diversity in glass compositions from Mentolat than have been previously reported and that magmas formed beneath Mentolat may follow distinct diversification pathways leading to greater chemical diversity in the evolved material from this center.

The morphological characteristics of the volcanic edifice also supports Mentolat as the source of the ~11.7 ka MEN tephra as opposed to Cay volcano which has also produced geochemically evolved amphibole-bearing eruptive material (Fig. 10). Cay lacks a summit crater and was heavily eroded during the last glaciation (Naranjo and Stern, 2004) suggesting that this center has had a quiescent eruptive history since

glacial retreat from the region and throughout the Holocene. In contrast Mentolat, has a large ice-filled summit crater (Naranjo and Stern, 2004) and has produced numerous amphibole-bearing explosive eruptions during the Holocene and as far back as the late-glacial time (Stern et al., 2016, 2015; Weller et al., 2015, 2017, 2018).

The spatial distribution of the ~11.7 ka MEN tephra indicates that the axis of dispersion for this eruption was directed to the southeast (Fig. 11) reaching a maximum thickness of ~13 cm at a distance of 95 km from the source vent. The thickness of this tephra in Lake Tranquilo (LTr in Fig. 1; Weller et al., 2015), located another 50 km to the southeast, is ~9 cm, much greater than the surrounding lake cores which are all 2 cm or less in thickness (Fig. 1; Table 1). Reworking could have led to thickening of this deposit compared to the original air fall thickness. Alternatively, Lake Tranquilo is located on the lee side of a topographic barrier, and Watt et al. (2015) demonstrated that tephra deposition can be enhanced when eruption plumes pass over regions with complex topography.

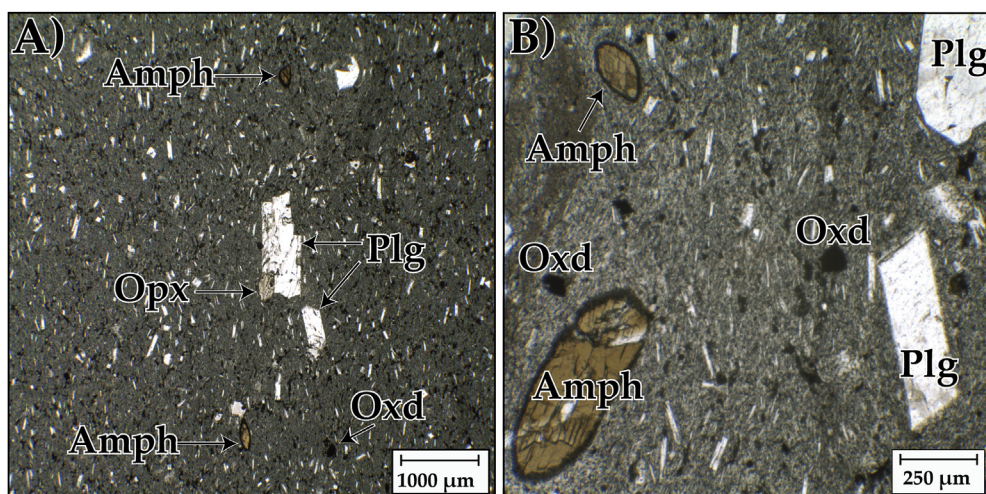


Fig. 10. Photomicrographs illustrating the phenocryst identity, the abundance of the mineral constituents and the textural features of the amphibole phenocrysts from the dacite which forms a small volcanic plug near the summit of Cay volcano. **A)** The dacite is relatively crystal-poor. It contains small phenocrysts of plagioclase (Plg), orthopyroxene (Opx), amphibole (Amph), and unidentified Fe-Ti oxides (Oxd), but not olivine and/or clinopyroxene as do the tephra from the ~11.7 ka MEN event. The groundmass contains abundant small microlites of plagioclase. **B)** The amphibole phenocrysts are scarce, typically small and have disequilibrium rims composed of fine-grained Fe-Ti oxides and plagioclase.

In the ~11.7 ka MEN tephra, amphiboles are observed in the dark grey, light grey, and white pumice lapilli indicating amphibole stability throughout the entire range of erupted material. This observation is supported by the wide range of pressures, temperatures, and melt H₂O contents, during amphibole crystallization (Fig. 8; Table 6). These estimates are wider than ranges for either Melimoyu or Cay, but are similar to the conditions during amphibole crystallization determined for other Mentolat-derived tephra. The presence of amphibole in the more mafic, dark grey compositions of the ~11.7 ka MEN tephra, and the formation of amphibole at relatively high pressures and temperatures, that are similar to amphiboles from other Mentolat-derived tephra, supports the suggestion of Weller and Stern (2018), that primitive magmas at Mentolat have higher volatile contents than the other SSVZ centers, which may be the result of the heightened delivery of water and other volatiles into the source region due to the subducting Guamblin Fracture Zone beneath this center. The presence of amphibole phenocrysts which lack oxidation textures in these tephra is distinct from those within the Cay dacite, which only has a minor proportion of small amphibole phenocrysts all with oxidation rims (Fig. 10B). One of the interesting distinctions between the amphiboles from the ~11.7 ka MEN tephra compared to those from the other Mentolat-derived tephra is the small difference in the estimated f_{O_2} (Fig. 8) with the majority of the amphiboles from Mentolat forming at an f_{O_2} just above the NNO + 1 oxygen buffer and the amphiboles from the ~11.7 ka MEN tephra having somewhat lower oxygen fugacity just below the NNO + 1 buffer.

The ~11.7 ka MEN tephra represent a significant event in the eruptive history of Mentolat because of its relatively large size with an estimated eruptive volume of 1.8 km³ (Fig. 11) and an eruption magnitude of 5.2 (Pyle, 2015). This event was larger than the May 2008 Chaitén eruption (Alfano et al., 2011; Watt et al., 2009) but was smaller than the Ho, H1, H2 and the 1991 AD events of Hudson volcano (Naranjo and Stern, 1998; Scasso et al., 1994; Stern, 1991; Weller et al., 2014) and the 1932 eruption of Quizapu volcano (Hildreth and Drake, 1992).

Throughout the late Pleistocene and Holocene, Mentolat has

Table 6

Summary of the physical and chemical conditions of amphibole crystallization from the ~11.7 ka MEN tephra and others derived from Mentolat and the other southernmost SSVZ centers.

Volcano	Tephra	Material	n	T (°C)	P (MPa)	ΔNNO	H ₂ O _{melt} (wt.%)
Mentolat	RM and MET	Tephra	38	834–969	154–406	0.3–1.2	4.9–7.0
Mentolat	B2, D1, I, Q3, and MENO	Tephra	58	832–1014	128–579	0.6–1.6	4.4–7.8
Melimoyu	MEL1 and MEL2	Tephra	20	898–967	198–376	–0.1–0.8	4.1–5.8
Cay	–	Lava	8	870–917	193–264	0.5–0.7	5.1–5.6

Table 7

Summary of the phenocryst geochemistry from the ~11.7 ka MEN tephra and the crustal xenoliths.

Phase	Material	n			
			En	Wo	Fs
Clinopyroxene	Phenocrysts	7	41.0 – 43.7	39.8 – 44.6	13.1 – 16.5
Orthopyroxene	Phenocrysts	8	59.0 – 71.8	1.7 – 2.7	25.5 – 39.3
			Fo	Fa	
Olivine	Phenocrysts	5	70.9 – 77.8	22.2 – 28.8	
			An	Ab	Or
Plagioclase	Phenocrysts	7	26.1 – 38.9	59.4 – 71.9	1.24 – 2.39
Plagioclase	Xenolith	6	21.8 – 32.2	67.4 – 77.6	0.38 – 0.76

produced approximately eighteen explosive eruptions (Stern et al., 2016, 2015; Weller et al., 2018, 2017, 2015). These eruptions include the ~7700 cal years BP MEN1 event that was dispersed primarily to the south and is observed in lacustrine sediment cores and subaerial soil sequences near the town of Cochrane (McCulloch et al., 2016; Stern et al., 2016) and in proximal soil exposure near Puerto Aisén (Naranjo and Stern, 2004), and the ~18,672 cal years BP MENO tephra that is observed in lacustrine sediment cores near the town of Coyhaique (Weller et al., 2018, 2015). The MEN1 and MENO events, were likely as large, if not larger than the eruption that produced the ~11.7 ka MEN tephra.

5. Conclusion

The tephra in the Mallín el Toqui (MET) lacustrine sediment core and the Río Maniguales (RM) outcrop preserve evidence for a large explosive eruption of Mentolat volcano that is constrained in age at ≥11,728 cal years BP. These tephra are composed of pumice lapilli that ranges in color from dark grey to white containing abundant phenocrysts of amphibole, plagioclase, orthopyroxene, clinopyroxene,

Table 8
New radiocarbon age determinations from the Mallín el Toqui lacustrine sediment core.

Laboratory No.	Core	Section	Depth (cm)	Material	¹⁴ C yrs BP	cal yrs BP	1 sigma error
D-AMS 017349	0115	AT2B	26–27	Organic/sediment	1522	1355	19
D-AMS 017350	0115	AT5B	36–37	Organic/sediment	1705	1564	23
D-AMS 017351	0115	AT7T	45–46	Organic/sediment	6506	7373	27
D-AMS 017352	0115	AT8B	35–36	Organic/sediment	8048	8875	39
D-AMS 017353	0115	AT10T	13–14	Sediment	10,109	11,728	34

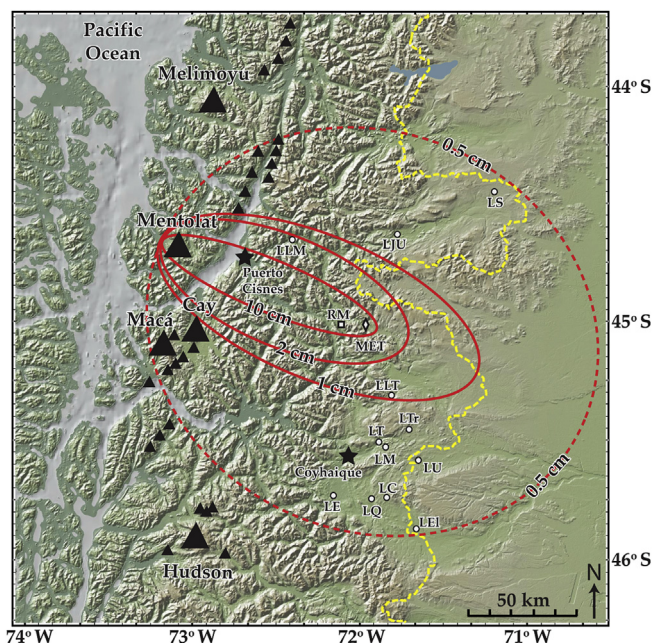


Fig. 11. Solid lines show the estimated 10-, 2-, and 1-cm isopachs of the ~11.7 ka MEN eruption. The dashed line shows the poorly constrained maximum extent of the 0.5 cm isopach. The location of the lacustrine sediment cores and RM and MET sites are indicated. The isopachs indicate that the eruption plume was dispersed predominately to southeast.

and minor olivine, Fe-Ti oxides, and crustal xenoliths. The pumice lapilli range from 58 up to 76 wt. % SiO₂ are medium-to low-K₂O calc-alkaline compositions. The pumice components have the Very Low Abundance (VLA)-type character similar to tephra and lava derived from Mentolat. The amphiboles from these tephtras are similar compositionally and formed over a wide range of temperatures (834–969 °C), pressures (154–406 MPa), and melt water contents (4.9–7.0 wt. %) that are similar to amphiboles from other Mentolat tephtras.

Based on its age and geochemistry, the MET and RM tephtras are correlative with other Mentolat-derived tephtras of similar age described from the region and is termed the ~11.7 ka MEN eruption. Mentolat has produced numerous (> 18) large explosive eruptions since glacial retreat and future eruptions from this center could impact local population centers and the agricultural industry in Chile and Argentina. Furthermore, this eruption represents an important chronological tephtra marker for future paleoclimate, paleoecologic, and archeological studies in this region.

Acknowledgements

This research was supported by FONDECYT-Chile grant #1130128, Regional Fondecyt Program R17A10002, and the National Science Foundation (EAR1427626). We would like to express our gratitude to Paulo Coutinho for assistance in the laboratory, and the Hospital Público San Juan de Dios (La Serena) for facilities to take the digital X-radiographs of the cores. We would like to thank Sebastian Watt and

Jose Antonio Naranjo for their constructive reviews of this manuscript.

Appendix A. Supplementary data

Supplementary data associated with this article can be found, in the online version, at <https://doi.org/10.1016/j.jsames.2018.12.020>.

References

- Alfano, F., Bonadonna, C., Volentik, A.C.M., Connor, C.B., Watt, S.F.L., Pyle, D.M., Connor, L.J., 2011. Tephra stratigraphy and eruptive volume of the May, 2008, Chaitén eruption, Chile. *Bull. Volcanol.* 73, 613–630. <https://doi.org/10.1007/s00445-010-0428-x>.
- Alloway, B.V., Pearce, N.J.G., Moreno, P.I., Villarosa, G., Jara, I., De Pol-Holz, R., Outes, V., 2017. An 18,000 year-long eruptive record from Volcán Chaitén, northwestern Patagonia: Paleoenvironmental and hazard-assessment implications. *Quat. Sci. Rev.* 168, 151–181. <https://doi.org/10.1016/j.quascirev.2017.05.011>.
- Bendle, J.M., Palmer, A.P., Thorndyraft, V.R., Matthews, I.P., 2017. High-resolution chronology for deglaciation of the Patagonian Ice Sheet at Lago Buenos Aires (46.5°S) revealed through varve chronology and Bayesian age modelling. *Quat. Sci. Rev.* 177, 314–339. <https://doi.org/10.1016/j.quascirev.2017.10.013>.
- Bertrand, S., Araneda, A., Vargas, P., Jana, P., Fagel, N., Urrutia, R., 2012. Using the N/C ratio to correct bulk radiocarbon ages from lake sediments: Insights from Chilean Patagonia. *Quat. Geochronol.* 12, 23–29. <https://doi.org/10.1016/j.quageo.2012.06.003>.
- Bertrand, S., Daga, R., Bedert, R., Fontijn, K., 2014. Deposition of the 2011–2012 Cordón Caulle tephra (Chile, 40°S) in lake sediments: Implications for tephrochronology and volcanology. *J. Geophys. Res.* Earth Surf. 2555–2573. (Received). <https://doi.org/10.1002/2014JF003321>.
- Cande, S.C., Leslie, R.B., 1986. Late Cenozoic Tectonics of the Southern Chile Trench. *J. Geophys. Res.* 91, 471–496.
- Cande, S.C., Leslie, R.B., Parra, J.C., Hobart, M., 1987. Interaction between the Chile Ridge and Chile Trench. *Geophys. Geoth. Evid.* 92, 495–520.
- Cembrano, J., Hervé, F., Lavenu, A., 1996. The Liquifite Ofqui fault zone: a long-lived intra-arc fault system in southern Chile. *Tectonophysics* 1, 55–66.
- D’Orazio, M., Innocenti, F., Manetti, P., Tamponi, M., Tonarini, S., González-Ferrán, O., Lahsen, A., Omarini, R., 2003. The Quaternary calc-alkaline volcanism of the Patagonian Andes close to the Chile triple junction: Geochemistry and petrogenesis of volcanic rocks from the Cay and Maca volcanoes (~ 45°S, Chile). *J. South Am. Earth Sci.* 16, 219–242. [https://doi.org/10.1016/S0895-9811\(03\)00063-4](https://doi.org/10.1016/S0895-9811(03)00063-4).
- de Porras, M.E., Maldonado, A., Abarzúa, A.M., Cárdenas, M.L., Franco, J.P., Martel-Cea, A., Stern, C.R., Méndez, C., Reyes, O., 2012. Postglacial vegetation, fire and climate dynamics at Central Chilean Patagonia (Lake Shaman, 44°S). *Quat. Sci. Rev.* 50, 71–85. <https://doi.org/10.1016/j.quascirev.2012.06.015>.
- de Porras, M.E., Maldonado, A., Quintana, F.A., Martel-Cea, A., Reyes, O., Méndez, C., 2014. Environmental and climatic changes in central Chilean Patagonia since the Late Glacial (Mallín El Embudo, 44° S). *Clim. Past* 10, 1063–1078. <https://doi.org/10.5194/cp-10-1063-2014>.
- DeMets, C., Gordon, R.G., Argus, D.F., 2010. Geologically current plate motions. *Geophys. J. Int.* 181, 1–80. <https://doi.org/10.1111/j.1365-246X.2009.04491.x>.
- Elbert, J., Wartenburger, R., von Gunten, L., Urrutia, R., Fischer, D., Fajak, M., Hamann, Y., Greber, N.D., Grosjean, M., 2013. Late Holocene air temperature variability reconstructed from the sediments of Laguna Escondida, Patagonia, Chile (45°30’S). *Palaeogeogr. Palaeoclimatol. Palaeoecol.* 369, 482–492. <https://doi.org/10.1016/j.palaeo.2012.11.013>.
- Ewart, A., 1982. The mineralogy and petrology of Tertiary-Recent orogenic volcanic rocks: with special reference to the andesitic-basaltic compositional range. In: Thorpe, R.S. (Ed.), *Andesites: Orogenic Andesites and Related Rocks*. John Wiley & Sons, Chichester, pp. 25–95.
- Fagel, N., Alvarez, D., Namur, O., Devidal, J.-L., Nuttin, L., Schmidt, S., Jana, P., Torrejon, F., Bertrand, S., Araneda, A., Urrutia, R., 2017. Lacustrine record of last millennia eruptions in Northern Chilean Patagonia (45–47°S). *The Holocene* 27, 1227–1251. <https://doi.org/10.1177/09596836166687380>.
- Farmer, G.L., Broxton, D.E., Warren, R.G., Pickthorn, W., 1991. Nd, Sr, and O isotopic variations in metaluminous ash-flow tuffs and related volcanic rocks at the Timber Mountain/Oasis Valley Caldera, Complex, SW Nevada: implications for the origin and evolution of large-volume silicic magma bodies. *Contrib. Mineral. Petrol.* 109, 53–68. <https://doi.org/10.1007/BF00687200>.
- Fontijn, K., Lachowycz, S.M., Rawson, H., Pyle, D.M., Mather, T.A., Naranjo, J.A., Moreno-Roa, H., 2014. Late Quaternary tephrostratigraphy of southern Chile and

- Argentina. *Quat. Sci. Rev.* 89, 70–84. <https://doi.org/10.1016/j.quascirev.2014.02.007>.
- Futa, K., Stern, C.R., 1988. Sr and Nd isotopic and trace element compositions of Quaternary volcanic centers of the Southern Andes. *Earth Planet. Sci. Lett.* 88, 253–262. [https://doi.org/10.1016/0012-821X\(88\)90082-9](https://doi.org/10.1016/0012-821X(88)90082-9).
- Gutiérrez, F., Gioncada, A., González Ferran, O., Lahsen, A., Mazzuoli, R., 2005. The Hudson Volcano and surrounding monogenetic centres (Chilean Patagonia): An example of volcanism associated with ridge – trench collision environment. *J. Volcanol. Geotherm. Res.* 145, 207–233. <https://doi.org/10.1016/j.jvolgeores.2005.01.014>.
- Haberle, S.G., Lumley, S.H., 1998. Age and origin of tephra recorded in postglacial lake sediments to the west of the southern Andes, 44°S to 47°S. *J. Volcanol. Geotherm. Res.* 84, 239–256. [https://doi.org/10.1016/S0377-0273\(98\)00037-7](https://doi.org/10.1016/S0377-0273(98)00037-7).
- Hervé, F., Pankhurst, R.J., Drake, R., Beck, M.E., 1995. Pillow metabasalts in a mid-Tertiary extensional basin adjacent to the Liquiñe-Ofqui fault zone: the Isla Magdalena area, Aysén, Chile. *J. South Am. Earth Sci.* 8, 33–46. [https://doi.org/10.1016/0895-9811\(94\)00039-5](https://doi.org/10.1016/0895-9811(94)00039-5).
- Hervé, F., Pankhurst, R.J., Drake, R.E., Beck, M.E., 1993. Basic Magmatism in a Mid-Tertiary Transensional Basin, Magdalena, Isla. *J. South Am. Earth Sci.* 8, 21–23.
- Hickey-Vargas, R., Abdollahi, M.J., Parada, M.A., López-Escobar, L., Frey, F.A., 1995. Crustal xenoliths from Calbuco Volcano, Andean Southern Volcanic Zone: implications for crustal composition and magma-crust interaction. *Contrib. Mineral. Petrol.* 119, 331–344. <https://doi.org/10.1007/BF00286933>.
- Hildreth, W., Drake, R., 1992. Volcán Quizapu, Chilean Andes. *Bull. Volcanol.* 54, 93–125. <https://doi.org/10.1007/BF00278002>.
- Hogg, A.G., Hua, Q., Blackwell, P.G., Niu, M., Buck, C.E., Guilderson, T.P., Heaton, T.J., Palmer, J.G., Reimer, P.J., Reimer, R.W., Turney, C.S.M., Zimmerman, S.R.H., 2013. SHCal13 Southern Hemisphere Calibration, 0–50,000 Years cal BP. *Radiocarbon* 55, 1889–1903. https://doi.org/10.2458/azu_js_rc.55.16783.
- Kratzmann, D.J., Carey, S., Scasso, R., Naranjo, J.-A., 2009. Compositional variations and magma mixing in the 1991 eruptions of Hudson volcano, Chile. *Bull. Volcanol.* 71, 419–439. <https://doi.org/10.1007/s00445-008-0234-x>.
- Kratzmann, D.J., Carey, S., Scasso, R.A., Naranjo, J.A., 2010. Role of cryptic amphibole crystallization in magma differentiation at Hudson volcano, Southern Volcanic Zone, Chile. *Contrib. to Mineral. Petrol.* 159, 237–264. <https://doi.org/10.1007/s00410-009-0426-1>.
- Lahsen, A., González-Ferrán, O., Innocenti, F., Manetti, P., Mazzuoli, R., Omarini, R., Tamponi, M.S., 1997. New Occurrence of Orogenic Volcanism along Liquiñe-Ofqui Fault System: The Rio Pescado Volcanic Centers, Southern Andes (45°30' S, 73°04' W), Chile. *VIII Congr. Geológico Chil. Actas I* 108–112.
- Lahsen, A., Lopez-Escobar, L., Vergara, M., 1994. The Puyuhuapi Volcanic Group, southern Andes (44°20'S): Geological and Geochemical Antecedents. In: *7th Congreso Geológico Chileno*, pp. 1076–1079.
- López-Escobar, L., Cembrano, J., Moreno, H., 1995a. Geochemistry and tectonics of the Chilean southern Andes basaltic Quaternary volcanism (37–46°S). *Rev. Geol. Chile* 22, 219–234. <https://doi.org/10.5027/andgeoV22n2-a06>.
- López-Escobar, L., Kilian, R., Kempton, P.D., Tarihi, M., 1993. Petrography and geochemistry of Quaternary rocks from the Southern Volcanic Zone of the Andes between 41°30' and 46°00'S, Chile. *Rev. Geol. Chile* 20, 33–55.
- López-Escobar, L., Parada, M.A., Hickey-Vargas, R., Frey, F.A., Kempton, P.D., Moreno, H., 1995b. Calbuco Volcano and minor eruptive centers distributed along the Liquiñe-Ofqui Fault Zone, Chile (41°–42° S): contrasting origin of andesitic and basaltic magma in the Southern Volcanic Zone of the Andes. *Contrib. Mineral. Petrol.* 119, 345–361. <https://doi.org/10.1006/prep.2001.1489>.
- Lowe, D.J., 2011. Tephrochronology and its application: A review. *Quat. Geochronol.* 6, 107–153. <https://doi.org/10.1016/j.quageo.2010.08.003>.
- Martin, F.M., Todisco, D., Rodet, J., San Román, M., Morello, F., Prevosti, F., Stern, C., Borrero, L.A., 2015. Nuevas excavaciones en Cueva del Medio: Procesos de formación de la cueva y avances en los estudios de interacción entre cazadores-recolectores y fauna extinta (Pleistoceno Final, Patagonia Meridional). *Magallania* 43, 165–189. <https://doi.org/10.4067/S0718-22442015000100010>.
- McCulloch, R.D., Figuerero Torres, M.J., Mengoni Goñalons, G.L., Barclay, R., Mansilla, C., 2016. A Holocene record of environmental change from Río Zeballos, central Patagonia. *Holocene* 27, 941–950. <https://doi.org/10.1177/0959683616678460>.
- Naranjo, A., Servicio, E., Moreno, H., El, R., Nacional, S., 1993. La erupción del volcán Hudson en 1991 (46°S), Región XI, Aysén, Chile. In: *Mpodozis, C.M. (Ed.), Servicio Nacional de Geología y Minería, Santiago*, pp. 1–51.
- Naranjo, J.A., Singer, B.S., Jicha, B.R., Moreno, H., Lara, L.E., 2017. Holocene tephra succession of Puyehue-Cordón Caulle and Antillanca/Casablanca volcanic complexes, southern Andes (40–41°S). *J. Volcanol. Geotherm. Res.* 332, 109–128. <https://doi.org/10.1016/j.jvolgeores.2016.11.017>.
- Naranjo, J.A., Stern, C.R., 2004. Holocene tephrochronology of the southernmost part (42°30'–45°S) of the Andean Southern Volcanic Zone. *Rev. Geol. Chile* 31, 225–240. <https://doi.org/10.4067/S0716-02082004000200003>.
- Naranjo, J.A., Stern, C.R., 1998. Holocene explosive activity of Hudson Volcano, southern Andes. *Bull. Volcanol.* 59, 291–306. <https://doi.org/10.1007/s004450050193>.
- Notsu, K., López-escobar, L., Onuma, N., 1987. Along-arc variation of Sr-isotope composition in volcanic rocks from the Southern Andes (33°S–55°S). *Geochem. J.* 21, 307–313.
- Pankhurst, R.J., Weaver, S.D., Hervé, F., Larrondo, P., 1999. Mesozoic – Cenozoic evolution of the North Patagonian Batholith in Aysén, southern Chile. *J. Geol. Soc. London.* 156, 673–694.
- Prieto, A., Stern, C.R., Estévez, J.E., 2013. The peopling of the Fuego-Patagonian fjords by littoral hunter-gatherers after the mid-Holocene H1 eruption of Hudson Volcano. *Quat. Int.* 317, 3–13. <https://doi.org/10.1016/j.quaint.2013.06.024>.
- Pyle, D.M., 2015. Sizes of Volcanic Eruptions. In: *Sigurdsson, H. (Ed.), The Encyclopedia of Volcanoes*. Academic Press, pp. 257–264. <https://doi.org/10.1016/B978-0-12-385938-9.00013-4>.
- Rawson, H., Naranjo, J.A., Smith, V.C., Fontijn, K., Pyle, D.M., Mather, T.A., Moreno, H., 2015. The frequency and magnitude of post-glacial explosive eruptions at Volcán Mocho-Choshuenco, southern Chile. *J. Volcanol. Geotherm. Res.* 299, 103–129. <https://doi.org/10.1016/j.jvolgeores.2015.04.003>.
- Ridolfi, F., Renzulli, A., Puerini, M., 2010. Stability and chemical equilibrium of amphibole in calc-alkaline magmas: An overview, new thermobarometric formulations and application to subduction-related volcanoes. *Contrib. Mineral. Petrol.* 160, 45–66. <https://doi.org/10.1007/s00410-009-0465-7>.
- Rodríguez, C., Sellés, D., Dungan, M., Langmuir, C., Leeman, W., 2007. Adakitic dacites formed by intracrustal crystal fractionation of water-rich parent magmas at Nevado de Longaví volcano (36.2°S; Andean Southern Volcanic Zone, Central Chile). *J. Petrol.* 48, 2033–2061. <https://doi.org/10.1093/petrology/egm049>.
- Saadat, S., Stern, C.R., 2011. Petrochemistry and genesis of olivine basalts from small monogenetic parasitic cones of Bazman stratovolcano, Makran arc, southeastern Iran. *Lithos* 125, 607–619. <https://doi.org/10.1016/j.lithos.2011.03.014>.
- Scasso, R.A., Corbella, H., Tiberi, P., 1994. Sedimentological Analysis of the tephra from the 12–15 August 1991 eruption of Hudson volcano. *Bull. Volcanol.* 56, 121–132.
- Sellés, D., Rodríguez, C.A., Dungan, M.A., 2004. Geochemistry of Nevado de Longaví Volcano (36.2°S): a compositionally atypical arc volcano in the Southern Volcanic Zone of the Andes. *Andean Geol.* 31, 293–315. <https://doi.org/10.4090/juec.2008.v2n2.033040>.
- Stern, C., de Porras, M.E., Maldonado, A., 2015. Tephrochronology of the upper Río Cisnes valley (44°S), southern Chile. *Andean Geol.* 42, 173–189. <https://doi.org/10.5027/andgeoV42n2-a02>.
- Stern, C., Moreno, P.I., Henríquez, W.I., Villa-Martínez, R., Sagredo, E., Aravena, J.C., De Pol-Holz, R., 2016. Holocene tephrochronology around Cochran (~47° S), southern Chile. *Andean Geol.* 43, 1–19. <https://doi.org/10.5027/andgeoV43n1-a01>.
- Stern, C.R., 2008. Holocene tephrochronology record of large explosive eruptions in the southernmost Patagonian Andes. *Bull. Volcanol.* 70, 435–454. <https://doi.org/10.1007/s00445-007-0148-z>.
- Stern, C.R., 2004. Active Andean volcanism: its geologic and tectonic setting. *Rev. Geol. Chile* 31, 1–51. <https://doi.org/10.4067/S0716-02082004000200001>.
- Stern, C.R., 1991. Mid-holocene tephra on tierra del Fuego (54°S) derived from the Hudson Volcano (46°S): evidence for a large explosive eruption. *18, 7–11*.
- Stern, C.R., Weller, D.J., 2012. A Revised Age of 7430 ± 250 14 C yrs BP for the Very Large mid-Holocene Explosive H1 Eruption of the Hudson Volcano, Southern Chile. *13th Chil. Geol. Congr.* 878–879.
- Stuiver, M., Reimer, P.J., Braziunas, T.F., 1998. High-Precision Radiocarbon Age Calibration for Terrestrial and Marine Samples. *Radiocarbon* 40, 1127–1151. https://doi.org/10.2458/azu_js_rc.v40i3.3786.
- Van Daele, M., Bertrand, S., Meyer, I., Moernaut, J., Vandoorne, W., Siani, G., Tanghe, N., Ghazoui, Z., Pino, M., Urrutia, R., De Batist, M., 2016. Late Quaternary evolution of Lago Castor (Chile, 45.6°S): Timing of the deglaciation in northern Patagonia and evolution of the southern westerlies during the last 17 kyr. *Quat. Sci. Rev.* 133, 130–146. <https://doi.org/10.1016/j.quascirev.2015.12.021>.
- Vargas, G., Rebollo, S., Sepúlveda, S.A., Lahsen, A., Thiele, R., Townley, B., Padilla, C., Rauld, R., Herrera, M.J., Lara, M., 2013. Submarine earthquake rupture, active faulting and volcanism along the major Liquiñe-Ofqui Fault Zone and implications for seismic hazard assessment in the Patagonian Andes. *Andean Geol.* 40. <https://doi.org/10.5027/andgeoV40n1-a07>.
- Völker, D., Kutterolf, S., Wehrmann, H., 2011. Comparative mass balance of volcanic edifices at the southern volcanic zone of the Andes between 33°S and 46°S. *J. Volcanol. Geotherm. Res.* 205, 114–129. <https://doi.org/10.1016/j.jvolgeores.2011.03.011>.
- Watt, S.F.L., Gilbert, J.S., Folch, A., Phillips, J.C., Cai, X.M., 2015. An example of enhanced tephra deposition driven by topographically induced atmospheric turbulence. *Bull. Volcanol.* 77. <https://doi.org/10.1007/s00445-015-0927-x>.
- Watt, S.F.L., Pyle, D.M., Mather, T.A., 2011a. Geology, petrology and geochemistry of the dome complex of Huequi volcano, southern Chile. *Andean Geol.* 38, 335–348. <https://doi.org/10.5027/andgeoV38n2-a05>.
- Watt, S.F.L., Pyle, D.M., Mather, T.A., Martin, R.S., Matthews, N.E., 2009. Fallout and distribution of volcanic ash over Argentina following the May 2008 explosive eruption of Chaitén, Chile. *J. Geophys. Res. Solid Earth* 114, 1–11. <https://doi.org/10.1029/2008JB006219>.
- Watt, S.F.L., Pyle, D.M., Naranjo, J.A., Rosqvist, G., Mella, M., Mather, T.A., Moreno, H., 2011b. Holocene tephrochronology of the Hualaihue region (Andean southern volcanic zone, ~42° S), southern Chile. *Quat. Int.* 246, 324–343. <https://doi.org/10.1016/j.quaint.2011.05.029>.
- Weller, D.J., de Porras, M.E., Maldonado, A., Mendez, C., Stern, C.R., 2017. Holocene tephrochronology of the lower Río Cisnes valley, southern Chile. *Andean Geol.* 44, 229–248. <https://doi.org/10.5027/andgeoV44n3-a01>.
- Weller, D.J., de Porras, M.E., Maldonado, A., Méndez, C., Stern, C.R., 2018. New age controls on the tephrochronology of the southernmost Andean Southern Volcanic Zone, Chile. *Quat. Res.* 1–15. <https://doi.org/doi:10.1017/qua.2018.81>.
- Weller, D.J., Miranda, C.G., Moreno, P.I., Villa-Martínez, R., Stern, C.R., 2015. Tephrochronology of the southernmost Andean Southern Volcanic Zone, Chile. *Bull. Volcanol.* 77, 1–24. <https://doi.org/10.1007/s00445-015-0991-2>.
- Weller, D.J., Miranda, C.G., Moreno, P.I., Villa-Martínez, R., Stern, C.R., 2014. The large late-glacial Ho eruption of the Hudson volcano, southern Chile. *Bull. Volcanol.* 76, 1–18. <https://doi.org/10.1007/s00445-014-0831-9>.
- Weller, D.J., Stern, C.R., 2018. Along-strike variability of primitive magmas (major and volatile elements) inferred from olivine-hosted melt inclusions, southernmost Andean Southern Volcanic Zone, Chile. *Lithos* 296–299, 233–244. <https://doi.org/10.1016/j.lithos.2017.11.009>.

- Wilson, T., Cole, J., Johnston, D., Cronin, S., Stewart, C., Dantas, A., 2012. Short- and long-term evacuation of people and livestock during a volcanic crisis: lessons from the 1991 eruption of Volcan Hudson, Chile. *J. Appl. Volcanol.* 1, 2. <https://doi.org/10.1186/2191-5040-1-2>.
- Wilson, T.M., Cole, J.W., Stewart, C., Cronin, S.J., Johnston, D.M., 2011. Ash storms: impacts of wind-remobilised volcanic ash on rural communities and agriculture following the 1991 Hudson eruption, southern Patagonia, Chile. *Bull. Volcanol.* 73, 223–239. <https://doi.org/10.1007/s00445-010-0396-1>.
- Wright, H.E., 1967. A square-rod piston sampler for lake sediments. *J. Sediment. Res.* 37, 975–976. <https://doi.org/10.1306/74D71807-2B21-11D7-8648000102C1865D>.